Spring 2020

Investigation on the Morphology of Charge-Transfer Complexes in Low Density Polyethylene

Wade Korf

INVESTIGATION ON THE MORPHOLOGY OF CHARGE-TRANSFER COMPLEXES IN LOW DENSITY POLYETHYLENE

by

Wade Allen Korf

A Thesis
Submitted to the Graduate School,
the College of Arts and Sciences
and the School of Polymer Science and Engineering
at The University of Southern Mississippi
in Partial Fulfillment of the Requirements
for the Degree of Master of Science

Approved by:

Dr. Yoan Simon, Committee Chair
Dr. Sergei Nazarenko
Dr. Xiaodan Gu

Dr. Yoan Simon Committee Chair	Dr. Jeffrey Wiggins Director of School	Dr. Karen S. Coats Dean of the Graduate School

May 2020

ABSTRACT

Fillers are used ubiquitously throughout the fields of polymer and material science to overcome many inherent limitations to polymeric materials (i.e. poor stiffness or strength) and to expand their potential applications. There is a need to develop controllable particle architectures to better understand fundamental structure-property relationships in particle reinforced polymer composites. Charge-transfer complexes (CTCs) can assemble *in situ* into various needle and dendritic shapes via simple fabrication processes and at low loading levels. In this study, the effect of tetrathiafulvalene (TTF) and 7,7,8,8-tetracyanoquinodimethane (TCNQ) CTC crystallites of various shapes and sizes on composite mechanical properties was investigated in an LDPE (low density polyethylene) polymer matrix. The CTC morphology was selectively controlled via the concentration, compression-molding temperature, or cooling rate to form needle and highly branched dendritic micro-crystallites. Optical imaging was used visualize the microstructure of the CTC crystallites. Fourier-transform infrared spectroscopy (FTIR) was used to confirm complexation of the TTF-TCNQ via shifts in the aromatic C-H and nitrile stretches in the composite samples. Differential Scanning Calorimetry (DSC) and X-ray Diffraction (XRD) results show that the presence of the CTC inclusions does not affect LDPE crystallization. In general, there was no observed difference between in the modulus, yield stress, and ultimate tensile strength between controls and the composite samples cooled at their corresponding rates. However, the elongation at break for the dendritic composites appeared to decrease as a function of dendrite size. Interestingly in some cases, the mechanical properties had a slight dependence on the CTC concentration and not the particle morphology.

ACKNOWLEDGMENTS

First, I would like to express genuine appreciation for my thesis adviser Dr. Yoan Simon of the School of Polymer Science and Engineering at The University of Southern Mississippi (USM) for his guidance, encouragement, invaluable feedback, and continued support of my research goals during my time in his group. He allowed me to work independently and his door was always open to discuss my research and career aspirations. Secondly, I sincerely appreciate all members of the Simon Research Group for their willingness to share knowledge of the lab techniques and skills needed for my research. Additionally, I would like to thank my committee and all those members of the department who provided assistance and training during my time in the program. Lastly, I would like to thank my friends and family for supporting me during writing this thesis and for my career in general.

TABLE OF CONTENTS

LIST OF TABLES

LIST OF ILLUSTRATIONS

LIST OF SCHEMES

LIST OF ABBREVIATIONS

2D	two-dimensional
AgNPs-PVA	silver nanoparticles-poly(vinyl alcohol)
Avg.	average
Bis-GMA	bisphenol A-glycidyl methacrylate
CF	carbon fiber
C-H	carbon-hydrogen bond
cm^2	square centimeter
CT Band	charge-transfer band
CTC	charge-transfer complex
DLA	diffusion-limited aggregation
DSC	differential scanning calorimetry
EDX	energy-dispersive X-ray spectroscopy
FTIR	Fourier-transform infrared spectroscopy
FWHM	full width at half maximum
g	grams
GPa	gigapascal
HOMO	highest occupied molecular orbital
J	joules
LDPE	low density polyethylene
LUMO	lowest unoccupied molecular orbital
mg	milligram
mL	milliliter

mm^2	square millimeter
μm	micrometers
MPa	megapascals
PC	polycarbonate
PMMA	polymethyl methacrylate
PVDF	polyvinylidene fluoride
RPU	rigid polyurethane
St. Dev.	standard deviation
TCNQ	7,7,8,8-tetracyanoquinodimethane
TEGDMA	triethylene glycol dimethacrylate
TTF	tetrathiafulvalene
TGA	thermogravimetric analysis
USM	University of Southern Mississippi
Wt. %	weight percent
XRD	X-ray Diffraction

CHAPTER I - INTRODUCTION

1.1 Charge-Transfer Complexes

Charge-transfer complexes (CTCs), or electron-donor-acceptor complexes, are stabilized molecular complexes formed by the weak electrostatic attraction of two or more molecules.[1] A charge donating source molecule called the electron donor transfers fractional electronic charges to a receiving molecule called the electron acceptor resulting in electronic transition into an excited electronic state and weak electron resonance between the two species as shown in ***Scheme 1.1.1*** below.[2] The electronic properties of

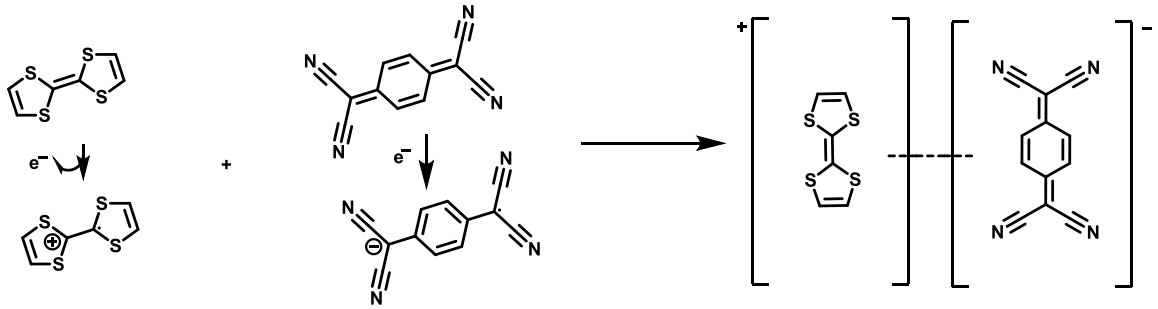

Scheme 1.1.1: Scheme illustrating TTF-TCNQ complexation.

CTCs are determined by the specific choice of the electron donor and acceptor molecules and their organization within a CTC complex. The energy gap between the highest occupied molecular orbital (HOMO) of the electron donor and the lowest unoccupied molecular orbital of the electron acceptor in a CTC is relatively small and results in an optical absorption band or charge-transfer band (CT band). The CTCs characteristic intense colors are reflected in the excitation energy of the resonance occurring frequently in the ultraviolet-visible or infrared regions of the electromagnetic spectrum.[3] Common electron

donor and electron acceptor molecules used to create charge-transfer salts are shown below in **Figure 1.1.1** and **Figure 1.1.2** respectively.[4]

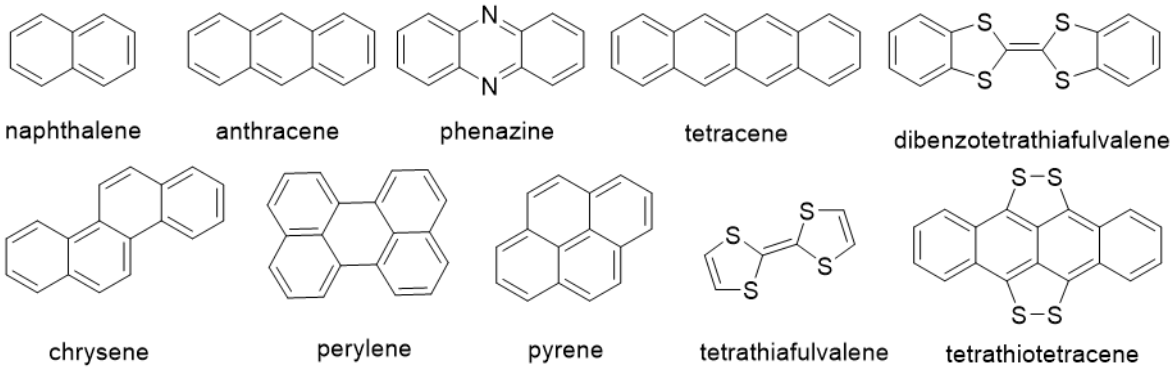

Figure 1.1.1: Common electron donors used in CTCs.

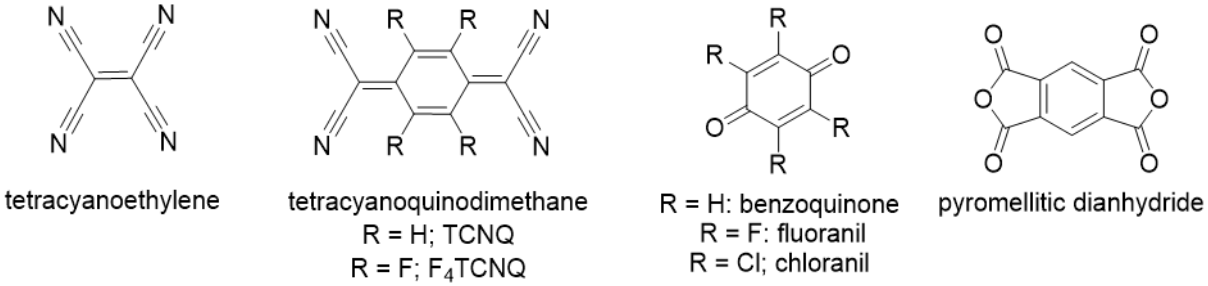

Figure 1.1.2: Electron acceptors commonly used in CTCs.

In the simplest case of a 1:1 ratio between the donor and acceptor, two different crystal packing geometries are commonly observed; mixed-stack and segregated-stack shown in **Figure 1.1.3**.[4] In the mixed-stack geometry the donor and acceptor alternate in

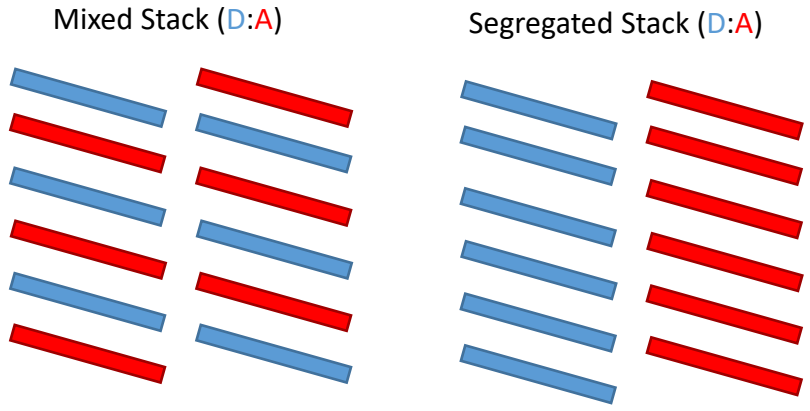

Figure 1.1.3: Mixed stack and segregated stack CTC geometries adapted from ref[4].

the π-stacking direction while in segregated-stack geometry the donor and acceptor π-stack separately as alternating columns. One of the most widely studied CTC, TTF-TCNQ, organizes into the segregated-stack geometry.[4] Several groups have studied the effect of various structures and morphologies of the CTC crystallites on conductivity. Kryszewski et al. used a solution casting process to form highly branched dendritic CTC particles in PC and PMMA films as shown in **Figure 1.1.4a**.[5] Similarly, Liu et al. used a 2-phase solution mixing method to vary the morphology TTF-TCNQ nanocrystals from straight nanowires to helical dendrites as seen in **Figure 1.1.4b** below.[6] Additionally, Tracz et al. formed reticulate-doped CTCs throughout polycarbonate films by studying the effects of

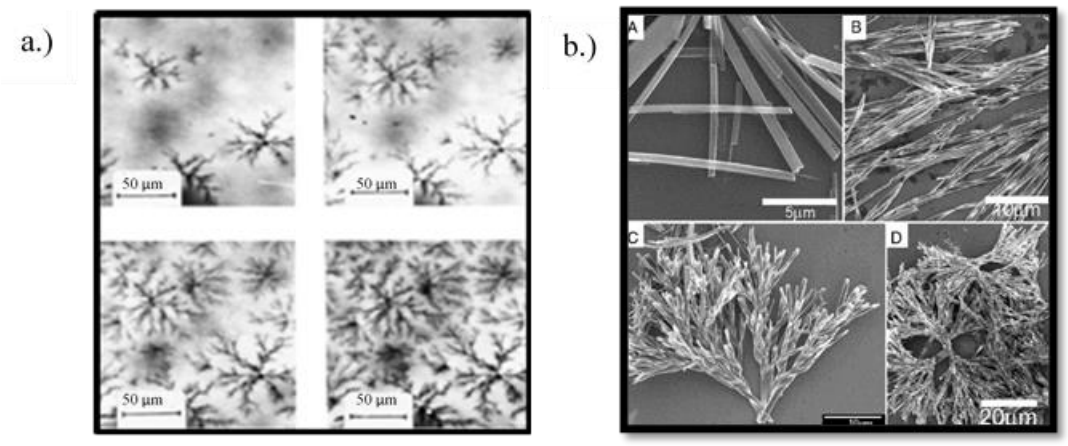

Figure 1.1.4: (a) Dendritic CTCs formed by solution casting in PC or PMMA from ref[5].(b) TTF-TCNQ nanocrystal morphologies formed via 2-phase mixing method from ref[6].

casting temperature and solvent.[7]

The formation of dendritic crystallites is governed by a fast, non-equilibrium crystallization that occurs when the solution or polymer mediums viscosity is relatively high and limits diffusion of the charge-transfer molecules to the crystallization front of already grown crystals and induces secondary nucleation on the crystal faces and subsequent branching.[5] Diffusion-limited aggregation (DLA) clusters form fractal-like

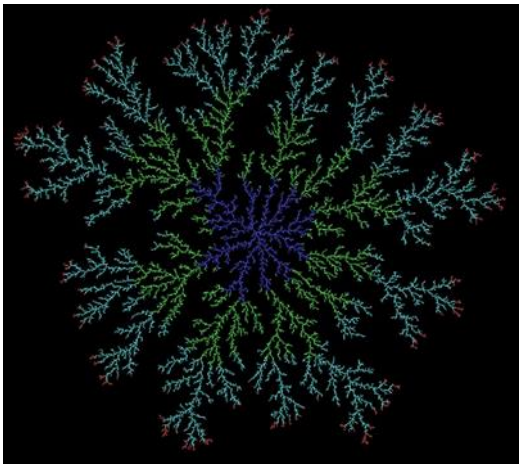

Figure 1.1.5: Image of a DLA Brownian tree simulation.

patterns called Brownian Trees as shown in **Figure 1.1.5** below via the random movement of molecules caused by thermal energy.[8] A concentration gradient between the supersaturated charge-transfer complex in the bulk and the equilibrium concentration at the crystal surface drives the diffusion process.[8] Since the molecular complex is based on electrostatic associations and not the formation of a strong covalent bond, the crystal growth process is dependent on factors such as the temperature, concentration, and solvent/polymer identity.

CTCs have traditionally been used to impart conductivity in organic electronic applications. The Moore group restored conductivity to mechanically damaged electronic devices using microencapsulated TTF and TCNQ solutions which individually are non-conductive.[9] Current research on CTCs as small-molecule organic semiconductors include applications for organic field-effect transistors,[10] organic-photovoltaic cells,[11–13] and organic light emitting diodes.[14] Additionally, CTCs have been shown to possess various other unique properties related to their charge-transfer capability such as ferroelectric behavior,[15–17] magnetoconductance,[18] field emission,[19] and photo-switching and memory function.[20,21].

1.2 Polymer Matrix Composites

Composite materials are artificially designed multiphase materials consisting of two or more chemically distinct phases separated by an interface. The primary *matrix* phase which is continuous in character, holds the dispersed phase in place, and is responsible for load transfer.[22] The secondary *dispersed* phase is embedded within the matrix in a discontinuous fashion and typically acts as the load-bearing component.[22] A judicious combination of the materials can ideally results in properties (strength, stiffness, durability, etc.) exceeding its individual components. Polymer composites have traditionally been used in load-bearing applications and are desired for their high strength-to-weight ratio, high durability, low cost, and ease of manufacturability.

The reinforcing phase of polymer composites is commonly particulates, fibers, or laminates. Particles reinforced polymer composites can have spherical, cubic, platelet,

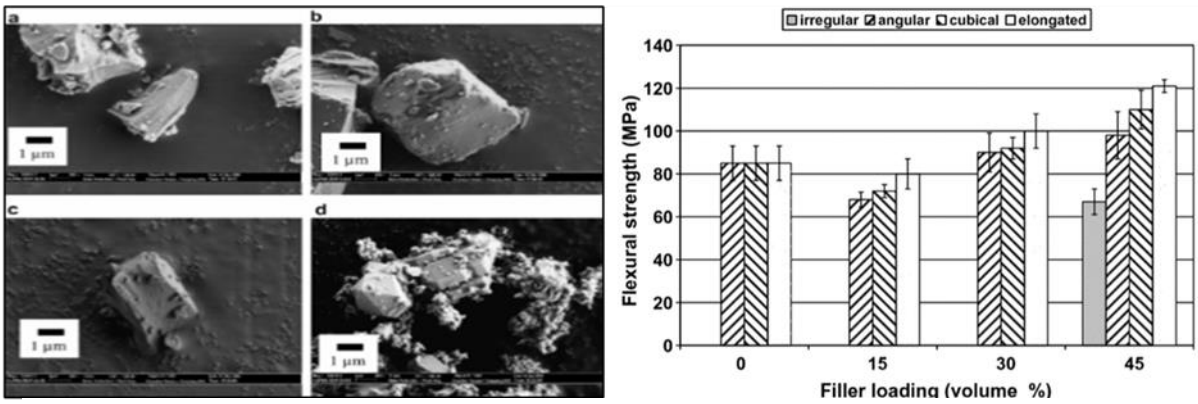

Figure 1.2.1: Effect of silica particles milled to different shapes from ref[23].

regular, or irregular geometries and typically have no preferred orientation.[22] Ahmad et al. established the increase in flexural strength at differ filler loading levels of a silica-filled epoxy composite of varying particle shape i.e. angular, cubic, elongated, and irregular as shown in **Figure 1.2.1**.[23] Similarly, Miyasaka observed an increase in composite strength as particle size decreased for different sized spherical and irregular quartz fillers in a

photocured matrix (bis-GMA and TEGDMA).[24] As seen in these studies, mechanical reinforcement is often dependent on the degree of surface interaction between matrix and filler and can be associated with its surface-to-volume ratio. Further, Ma et al. observed an increase in stiffness, strength, and toughness in a rigid polyurethane (RPU) matrix reinforced with dendritic short carbon fibers in comparison to pristine carbon fibers (CF) due to an increase in the fracture pathway as seen in **Figure 1.2.2** below.[25] The ability to control particle architecture has spurred additional research interests due to the fundamental and practical significance in composite material design.

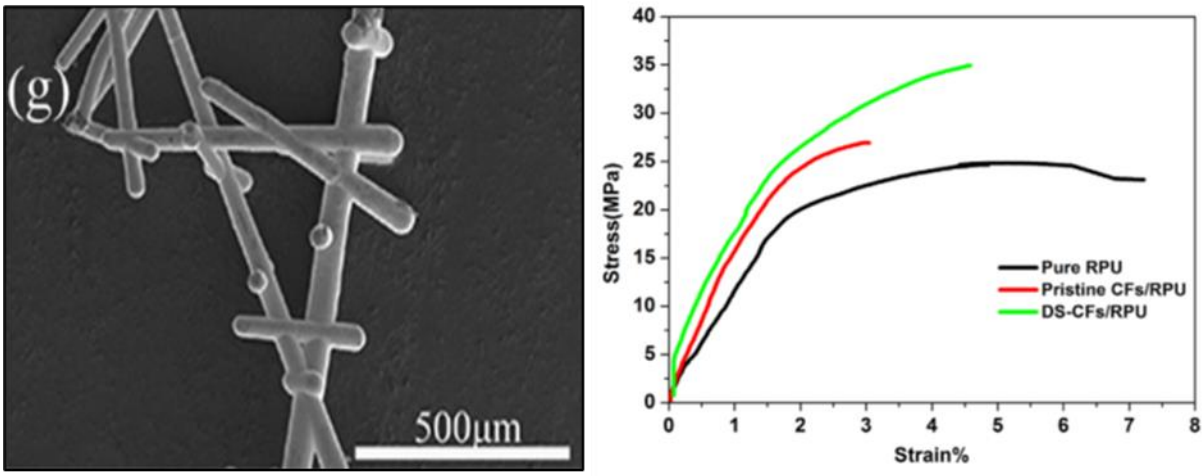

Figure 1.2.2: Dendritic short carbon fiber reinforcement for RPU matrix from ref [25].

The chemical and physical properties of composites is typically governed by its interfacial interactions of which there are two key types; matrix-filler and filler-filler.[26] Stress transfer between the matrix and filler is dependent on the level of interfacial adhesion and is described by the theory of adsorption.[27,28] In the absence of any chemically modified surface treatment, physisorption governs the strength of the interaction and is influenced by secondary forces (i.e. van der Waals). Sharpe introduced the idea of an interfacial region (an interphase) seen in **Figure 1.2.3** below with a gradient of properties different from that

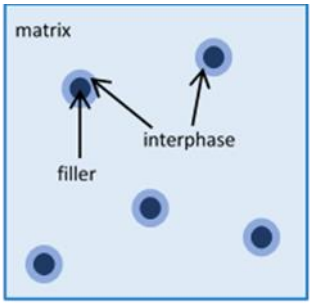

Figure 1.2.3: Image showing interphase region of particle reinforced matrix composite.

of the bulk filler and bulk matrix where the density, chain mobility, degree of cure, and transcrystallinity can be affected.[29,30] In **Figure 1.2.4** shown below, Zheng and coworkers observed transcrystallization of poly(vinylidene fluoride) (PVDF) in carbon fiber composites where crystallization is enhanced at the filler interface.[31] Conversely, the

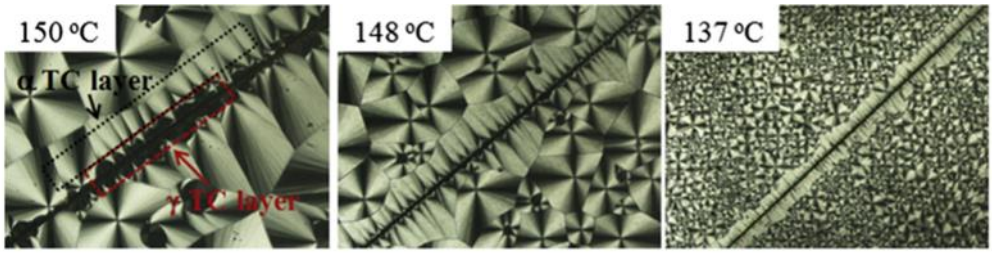

Figure 1.2.4: CF/PVDF composite showing transcrystalline regions from ref[31].

phenomenon of aggregation results in dense particle collectives where filler-filler type interactions are predominant. It has been widely shown that particle aggregates can cause lead to a deterioration of the mechanical properties due to a reduction in matrix-filler surface interactions or by introducing defects and areas of high stress concentration in the material as well as cause processing problems or poor aesthetics.[32–34] However, various reported studies have shown a reinforcing effect not attributed to classic matrix-filler interactions.[35–40] As shown in **Figure 1.2.5**, Tauban et al. demonstrated the dependence of composite mechanical properties on the complex geometries of the filler aggregates and their spatial arrangement.[40] Pioneering work by Dzenis[36] and Dorigato et al.[35] describe

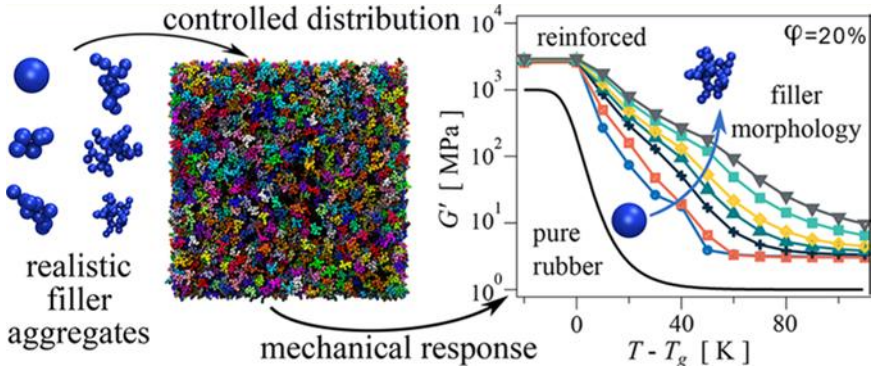

Figure 1.2.5: Image showing correlation between complex filler morphology and reinforcement from ref[40].

models where the unconstrained bulk polymer matrix can be subdivided into regions of constrained matrix and as shown in **Figure 1.2.6**. Deformation of the constrained matrix is impeded primarily by the presence of a rigid particle framework and additionally by

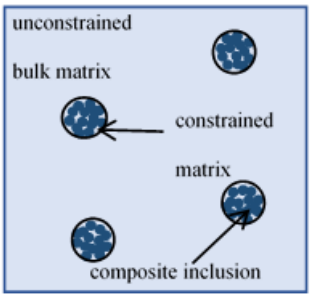

Figure 1.2.6: Image showing the constrained and unconstrained bulk matrix in a particle reinforced polymer composite.

entanglement of the polymer chains with the filler.[36,41] Therefore in these systems the particle morphology defines the volume of constrained matrix. The composite materials industry has various additional limitations that restrict their potential applications. Microcrystalline cellulose is often used as a reinforcing material, however it requires surface modification to improve particle dispersion.[42,43] The works by Miyasaka and Ahmad et al. discussed above only reach optimal mechanical performance at high inorganic filler loading levels (sometimes exceeding 45 vol. %) and this can potentially lead to challenges during composite processing.[23,24] Moreover, there are often expensive, difficult

to control, and complicated multi-step processes necessary in order to mill or synthesize complex particle architectures. The use of *in situ* compositing, where the fillers are synthesized internally in the matrix during composite fabrication is a current approach to overcoming many of those inherent limitations. Nanosized hydroxyapatite granules in chitosan films formed homogeneous and high strength composites via *in situ* compositing.[44] Li et al. synthesized spherical and rod-like Ag nanoparticle morphologies

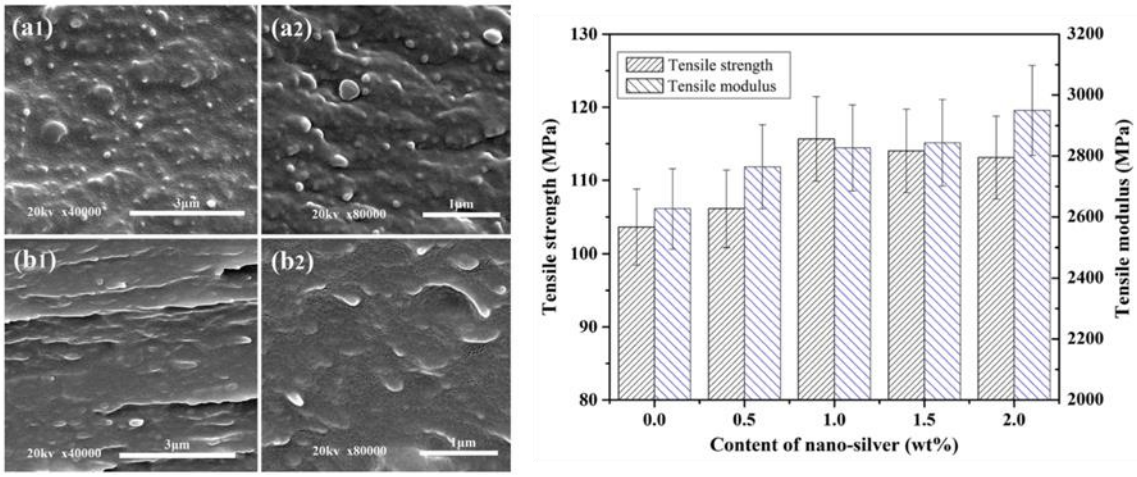

Figure 1.2.7: Spherical and rod-like Ag nanoparticle morphologies in silver-polyarylene ether nitrile nanocomposites from ref[45].

using *in situ* compositing as seen in **Figure 1.2.7** for the fabrication of silver-polyarylene ether nitrile nanocomposites of tunable mechanical properties.[45] Additionally, Selim et al. improved the pervaporation potentials of ethanol-water mixtures using the *in situ* generation technique for AgNPs-PVA.[46] In this thesis, the CTC architecture was selectively tuned *in situ* using a controllable melt-mixing process. The TTF-TCNQ is crystalline in nature and has previously been shown to have a Youngs modulus of ~20-55 GPa[47–50]. In the Ashby chart shown in **Figure 1.2.8** below, this is significantly higher than most

polymers indicating that if the matrix-filler interactions are compatible a reinforcing effect can be expected.[51]

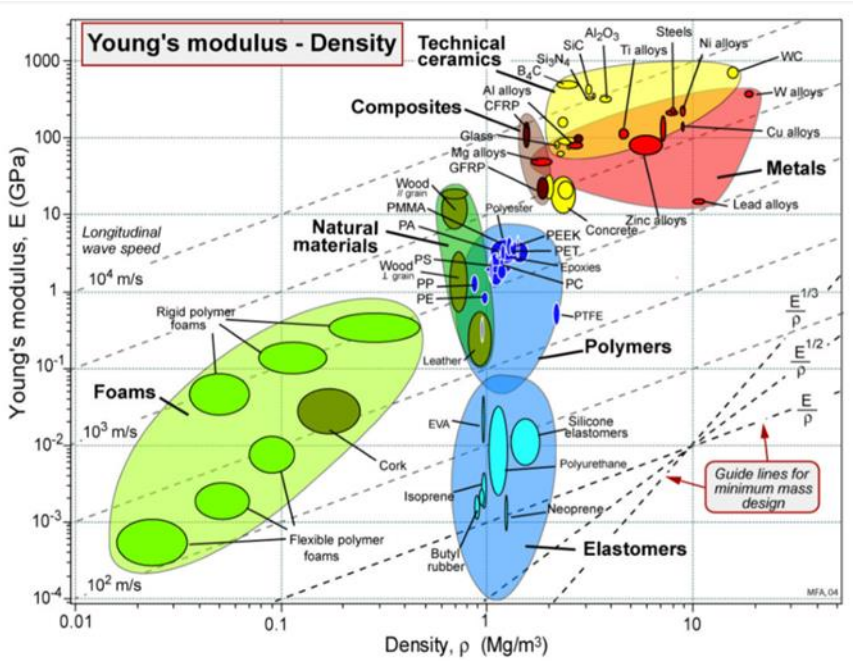

Figure 1.2.8: Ashby plot showing Young's modulus vs. Density of various groups of materials from ref[51].

CHAPTER II - EXPERIMENTAL METHODS

Melt-mixing Process:

Composite samples comprising the CTC and LDPE (DOW LDPE 133A or DOW LDPE 132I) were fabricated in a melt mixing process described below. Low-density polyethylene was used as the polymer matrix due to its hydrophobicity, melt processability, and because dendritic CTC particles have been previously shown to form in LDPE matrices.[52] The CTC used in this research is based on TTF and TCNQ as it is one of the most commonly studied CTCs and is relatively cost-effective (TTF ~$200/g; TCNQ ~$122/10g) in comparison to others. In a typical procedure, ~2.25g of the LDPE pellets were compression-molded in a Carver™ Model 4386 melt press for 10 seconds at 160 °C to form neat LDPE films transparent in appearance. The desired amount (0-2 wt.%) of TTF (orange powder) and TCNQ (brown/green crystals) were then measured out and pressed between two films under the same conditions in an effort to minimize loss of the CTC during handling as seen in **Figures 2.1 and 2.2**. The inhomogeneous film was then cut into pieces approximately <1 cm^2 before being transferred to a conical

Figure 2.1: Image showing TTF (orange) and TCNQ (greenish-brown) powders between two LDPE films prior to compression-molding.

Figure 2.2: Image showing the film after the initial press, the TTF and TCNQ are embedded in the LDPE matrix.

twin-screw Xplore™ MC5 Micro-Compounder for blending. The micro compounder was heated to 160 °C with a screw rotation speed of 160 rpm and a residence time of 3 minutes. The LDPE composite had a transparent yellow color immediately upon extruding and turned to a dark black color within 30 seconds upon cooling to room temperature as seen in **Figure 2.3** below. Neat LDPE was prepared in an identical manner without the CTC additives to make control samples.

Figure 2.3: Image showing transparent yellow composite extrudate cooling into a dark black/ brown color at room temperature.

Sample Preparation:

Figure 2.4: Mold for tensile bars between Teflon™ coated fiberglass sheets for ease of removal.

Approximately ~0.9g of the extruded filament was then placed in each dogbone mold as shown in **Figure 2.4** and compression molded for 3 minutes under 2 metric tons

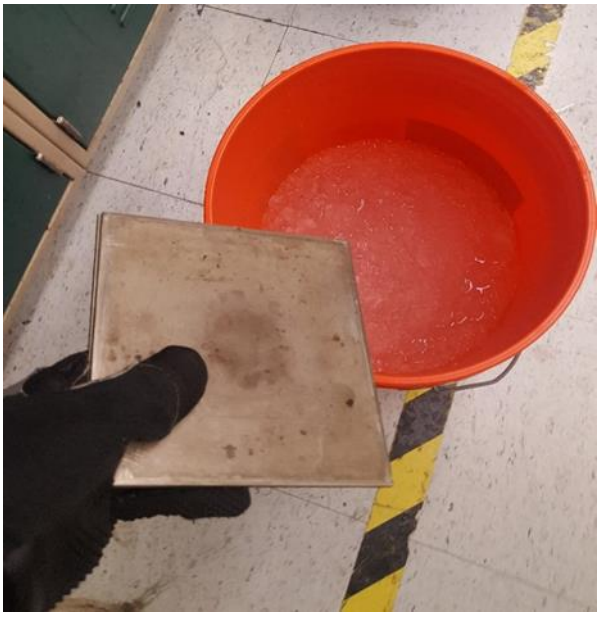

Figure 2.5: Fast cooled samples quenched in an ice-water bath.

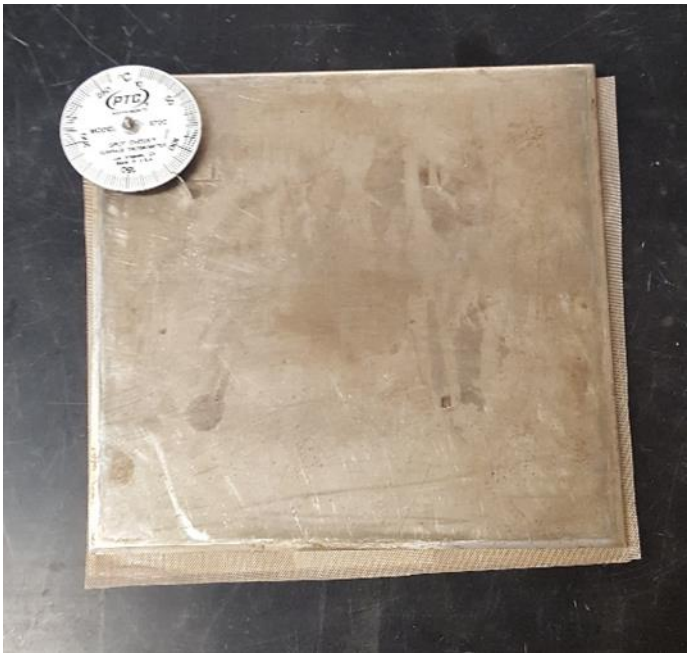

Figure 2.6: Normal cooled samples placed on the counter-top to cool.

of pressure at the designated temperature. The samples were then cooled at the desired rate and removed from the mold.

Figure 2.7: Slow cooled samples left on the Carver™ Melt-press as it cools to room temperature.

Three cooling speeds as shown in **Figures 2.5, 2.6, and 2.7** above were used in this study to control the CTC morphology; i.) quench cooled in an ice-water bath to minimize CTC crystallization where a greenish brown composite forms, ii.) normal cooled under ambient conditions on the counter-top to form small needle-like micro-crystals which appears as a light brownish color, and iii.) slow cooled on the melt-press as its cooled to room temperature over an hour where highly branched dendritic CTCs

Figure 2.8: Images showing the composite samples at the various cooling rates.

form seen as a speckled pattern. The temperature of the normal cooled samples was monitored via a PTC® Instruments Spot Check® Surface Thermometer. The optimal CTC weight % and melt press temperature was determined from an initial temperature vs concentration screening study- LDPE composites containing CTC weight fractions ranging from 0.15 – 2 wt. % were slowly cooled to room temperature over an hour from initial melt-press temperatures ranging from 120 °C to 190 °C. LDPE composites containing 0.25 wt. % CTC cooled slowly from 170 °C was chosen as a starting point based on the ability to form relatively large dendritic CTC microparticles. Upon quench-cooling the composite samples an inhomogeneous greenish-brown appearance forms, the normal cooled samples appear light brown, and the slowly cooled dendritic samples have a speckled pattern throughout as seen in **Figure 2.8** below.

Characterization:

Optical Imaging:

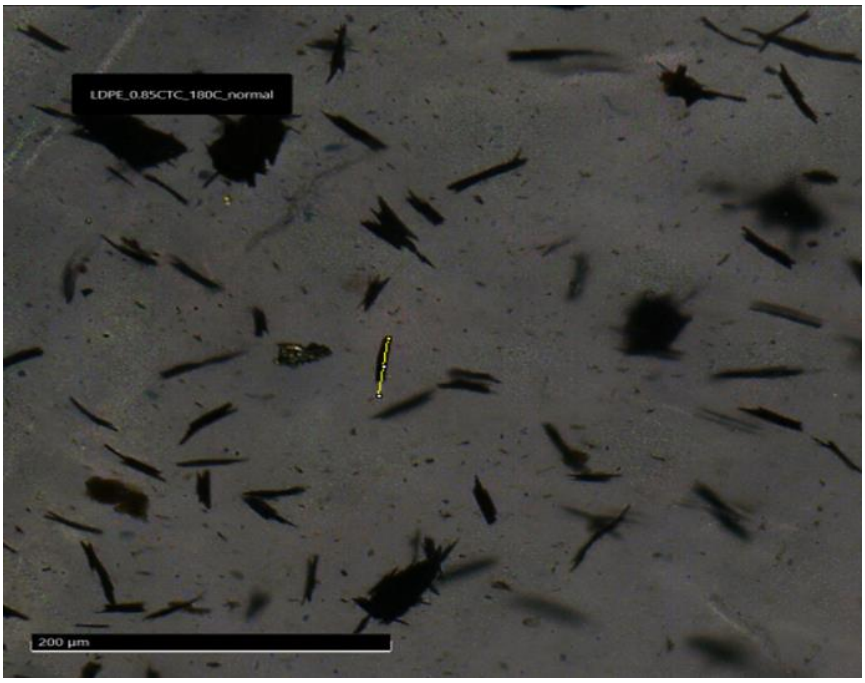

Figure 2.9: Representative image of LDPE_0.85CTC_180C_normal showing needle length measurement.

A Zeiss™ Smartzoom 5 microscope with Plano 5.0x, 1.6x, and 0.5x objectives was used to obtain optical images of the composite samples and to visualize the microstructure of the CTC crystallite particle inclusions. Additionally, the image analysis software ImageJ was used to measure the average diameter and length of the needle-like micro-crystallites, the longest diameter and radius of the dendritic inclusions, as well as estimate the average area, 2D number density, and 2D surface area fraction as shown in **Figures 2.9, 2.10.** and **2.11** respectively. The linear measurements were taken from an average of 10 particles, from only those crystallites that are in focus and not aggregated to adjacent crystals.

Figure 2.10: Representative image of longest diameter measurement of a dendritic CTC particle in LDPE_0.3CTC_180C_normal.

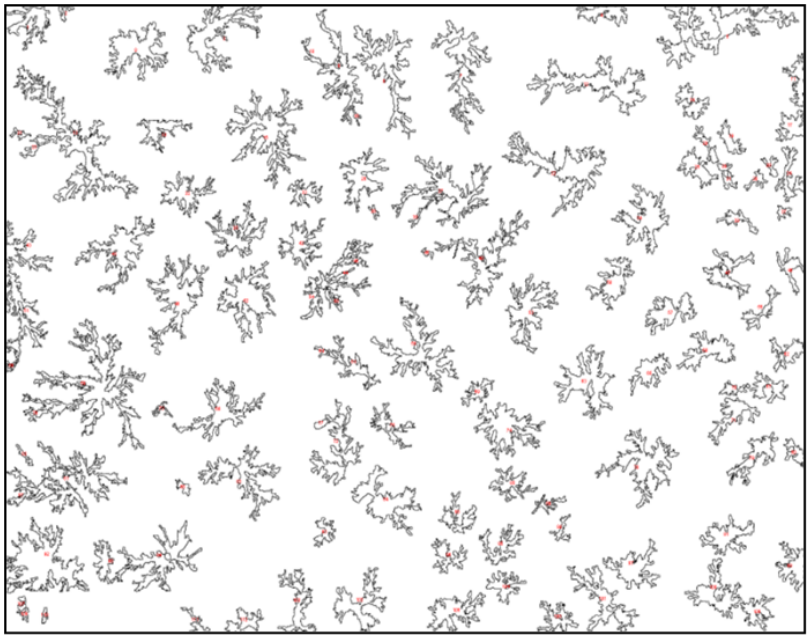

Figure 2.11: Representative image of LDPE_0.3CTC_180C_normal showing ImageJ particle analysis tool to determine average size, 2D surface area fraction, and 2D number density.

Fourier-Transform Infrared Spectroscopy (FTIR)

A PerkinElmer™ Frontier FT-IR Spectrometer was used to spectroscopically confirm the formation of the TTF-TCNQ complex in the composite samples. The TTF and TCNQ have been shown to readily complex in acetonitrile.[53] In a typical procedure, 20 mg of the TTF and TCNQ were dissolved separately in 10 mL of acetonitrile (2 mg/ mL), 5 mL of each were added to a new scintillation vial whereupon a black substance immediately began to precipitate out giving a visual indication of the complexation. The CTC was collected by gravity filtration and dried under vacuum. As shown in **Figure 2.12** the solid TCNQ appeared as fine greenish-brown crystals, the solid TTF appeared bright orange, whereas the CTC complex appeared black. The characteristic shifts observed from the parent TTF and TCNQ to the complexed TTF-TCNQ is then used to confirm complexation in the LDPE composite samples.

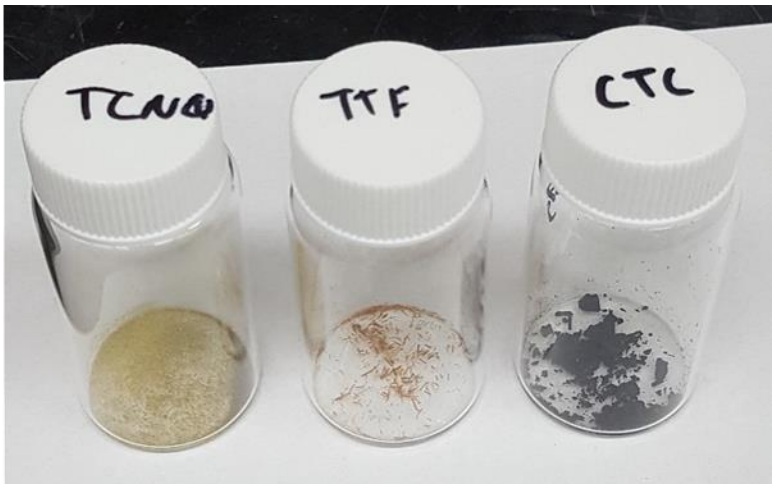

Figure 2.12: Image showing color differences between the parent TTF and TCNQ compounds versus the black complexed TTF-TCNQ (CTC).

Thermogravimetric Analysis (TGA)

Thermogravimetric analysis was performed using TA Instruments Q500 TGA on the three compounds shown above in **Figure 2.12** as well as the neat LDPE matrix to understand the thermal stability of the compounds during the melt-mixing and compression-molding processes. Approximately 5-25 mg of the samples were heated from 25 °C to 600 °C at 20 °C/min in the presence of an air atmosphere.

Differential Scanning Calorimetry (DSC)

A TA Instruments Q100 DSC was used to perform differential scanning calorimetry on the neat and composite LDPE samples at their respective cooling rates (slow, normal, fast) in order to determine the effect on the LDPE polymer matrix crystallinity. In a standard protocol, approximately 3-8 mg of the samples were heated from -80 °C to 200 °C at a ramp rate of 10 °C/min in a heat/cool/heat cycle and run in triplicate at a minimum. The enthalpy of fusion ΔH_f, is determined experimentally by integrating the endothermic melting peak from the initial heating cycle. While the theoretical enthalpy of fusion, ΔH_f^o is based on a 100% crystalline LDPE and is determined to be 293 J/g.[54] The degree of crystallinity is then estimated by normalizing the experimentally obtained ΔH_f to the theoretical ΔH_f^o as seen in **equation (2.1)** below.

$$\%\ crystallinity = \frac{\Delta H_f}{\Delta H_f^o} * 100\% \qquad \textbf{(2.1)}$$

X-ray Diffraction (XRD)

In conjunction with DSC, X-ray diffraction is another technique that is used to estimate the % crystallinity of the LDPE as well as the LDPE crystallite dimensions. A two-phase model is employed where the diffraction pattern is deconvoluted into the crystalline and amorphous regions using a gaussian fit function shown in **Figure 2.13** below where the full width at half max (FWHM) and peak areas can be determined.

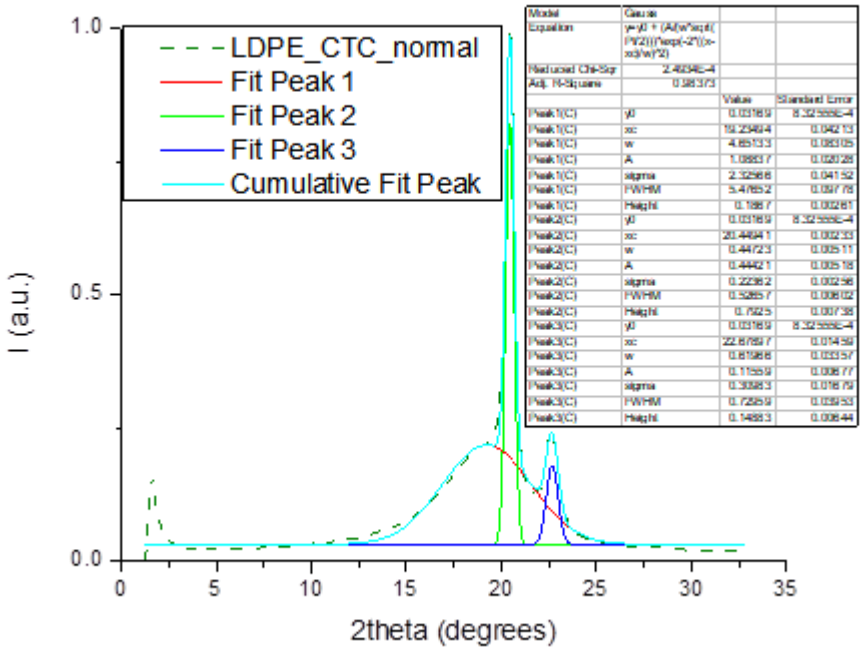

Figure 2.13: Representative plot of LDPE_CTC_normal showing deconvolution into amorphous (red) and crystalline (green and blue) regions.

The degree of crystallinity is determined by taking the ratio of the crystalline regions to the total area as seen in **equation (2.2)** below. Where I_c represents the scattering intensity of the crystalline peaks and I_a for the amorphous region respectively, and in this model the scattering intensity can be assumed proportional to the peak areas as found above.[55]

$$\%\ crystallinity = \left(\frac{I_c}{I_a + I_c}\right) * 100\% \qquad \textbf{(2.2)}$$

Similarly, the LDPE crystallite dimensions are determined for qualitative comparison using the Scherrer equation as shown below in **equation (2.3)** where the crystallite size L_{hkl} is inversely proportional to the FWHM, β (rad). Additionally, θ represents the Bragg angle of the *hkl* reflection, λ is the instrument wavelength (1.54 Å), and K is a dimensionless Scherrer constant assumed to be 0.9 for spherical crystals with cubic symmetry.[55]

$$L_{hkl} = \frac{K*\lambda}{\beta*cos\,(\theta)} \quad \textbf{(2.3)}$$

Tensile Testing

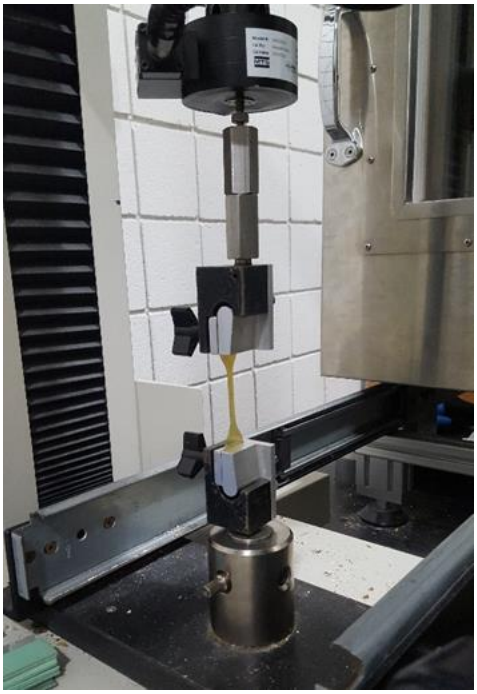

Figure 2.14: Representative tensile testing setup of LDPE_0.16CTC_180C_normal with DIN EN ISO 527-1 molded dog-bones.

Lastly, the mechanical properties of the composite and neat LDPE samples were measured using an MTS Insight® Electromechanical Testing System – 10 kN Standard

Length with a 500 N load cell attachment. Dog-bones were pressed according to DIN EN ISO 527-1 with cross-section of approximately 6 mm x 0.4 mm (width x thickness) as seen in **Figure 2.14** below. The samples were run in sets of 5 and a strain rate of 50 mm/min was used throughout. The average Young's Modulus, stress at yield, maximum strength, and strain at break were determined and compared.

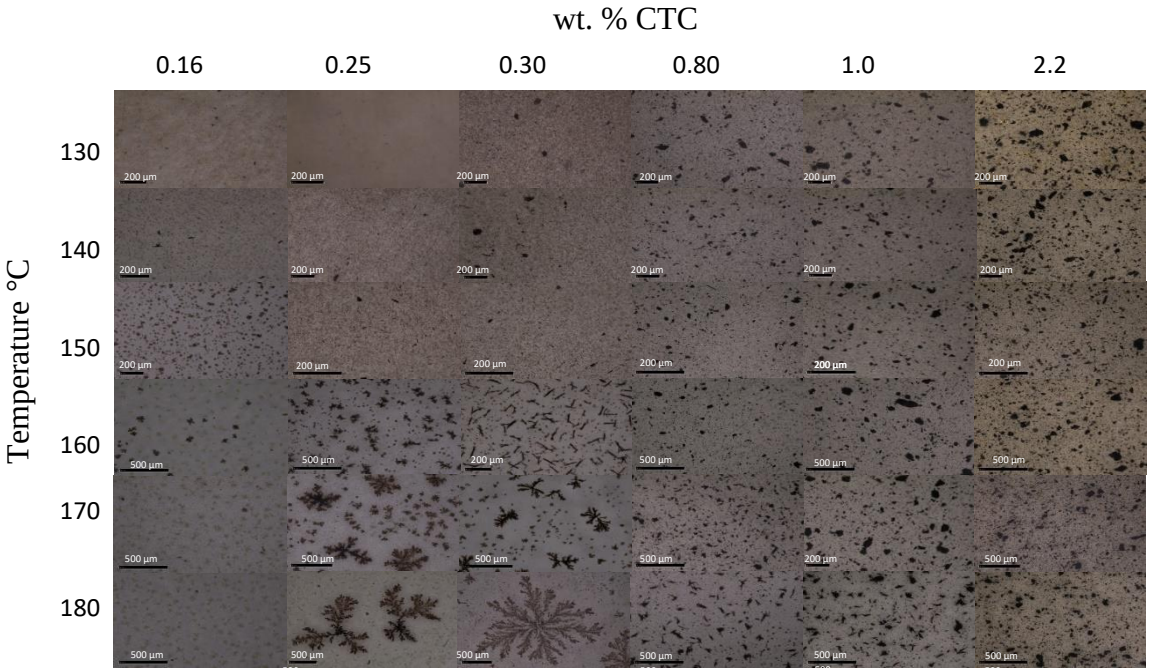

Figure 3.1: Optical images showing CTC morphologies formed in the slowly cooled samples with CTC weight percentage's 0.16 – 2.2 as a function of compression-molding temperature.

An initial temperature vs. concentration screening study was performed to determine the optimal weight percent CTC and compression-molding temperature to form dendritic micro-crystallites upon slowly cooling. As seen in **Figure 3.1** above the CTC inclusions appear as dark colored micro-crystallites, for larger CTC concentrations of 0.8 and above only needle-like crystals were observed indicating at high concentrations dendrite growth is not favored. Similarly, for samples cooled at compression-molding temperatures below 160 °C no dendrite formation occurred potentially indicating the viscosity of the LDPE matrix is too high and limits the diffusion of the TTF and TCNQ molecules to the growing crystal fronts. For the smallest concentration studied, 0.16 wt. %, dendrite growth appeared minimal indicating a lower

concentration threshold exists where crystal growth is inhibited as the distance between TTF and TCNQ molecules increases. Among the 0.25 and 0.30 wt. % samples, the dendrites appeared to grow in size as the initial compression-molding temperature increases reaching a peak at 180 °C however the very large leafy dendrites appeared inhomogeneously dispersed throughout. Ultimately a concentration of 0.25 wt. % and compression-molding temperature of 170 °C were chosen for further analysis.

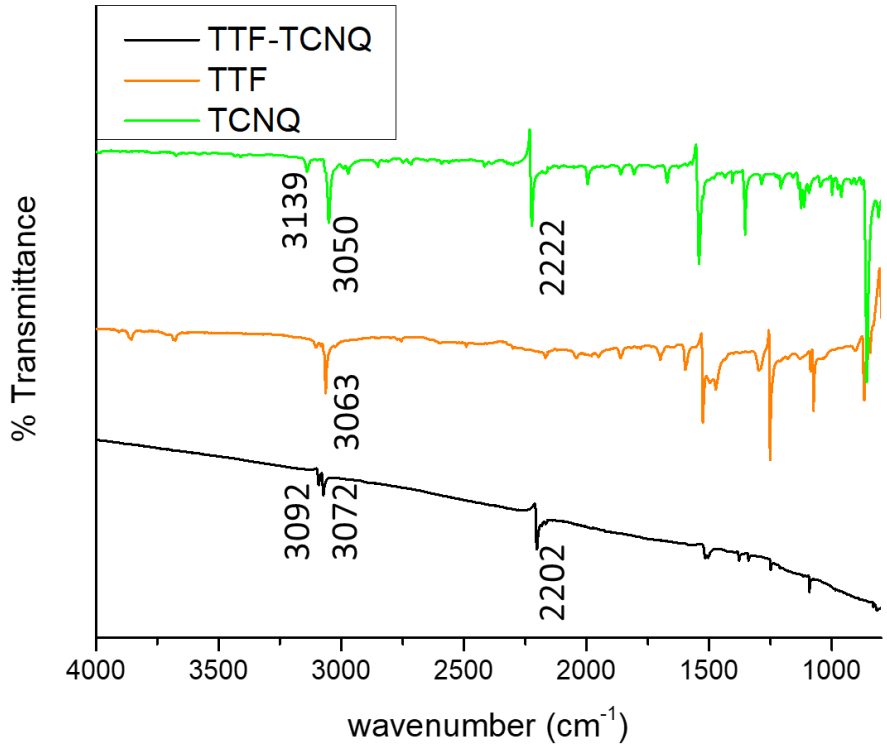

Figure 3.2: Overlay of FTIR spectra of TTF (orange curve), TCNQ (green curve), and TTF-TCNQ (black curve).

Table 3.1: Characteristic peaks of the aromatic C-H bond and Nitrile stretch in TTF, TCNQ, and TTF-TCNQ.

	C-H stretch	C-H stretch	Nitrile stretch
TTF	3063 cm-1		
TCNQ	3139 cm-1	3050 cm-1	2222 cm-1
TTF-TCNQ	3092 cm-1	3072 cm-1	2202 cm-1

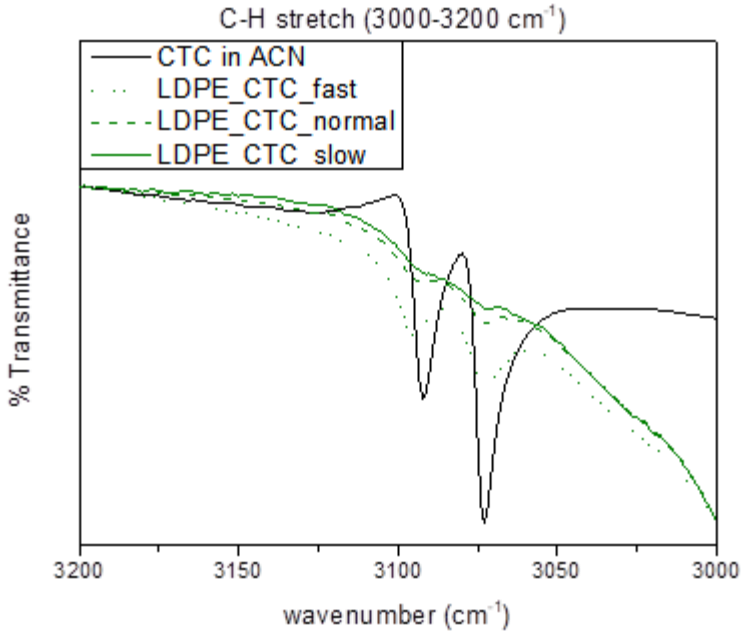

Figure 3.3: Overlayed FTIR spectra showing C-H stretch of the composite samples cooled at slow, normal, and fast speeds with the CTC crystallized from acetonitrile.

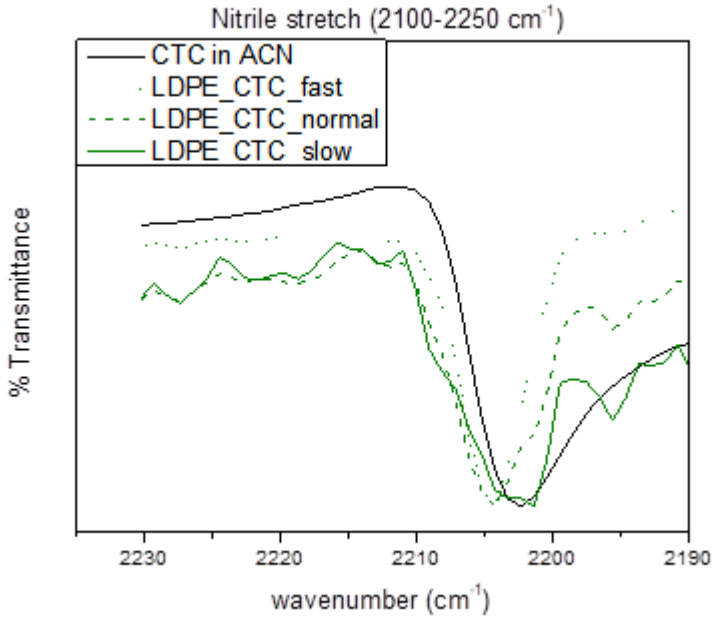

Figure 3.4: Overlayed FTIR spectra showing nitrile stretch of the composite samples cooled at slow, normal, and fast speeds with the CTC crystallized from acetonitrile.

FTIR spectroscopy was first performed on the parent TTF and TCNQ molecules as well as the CTC formed in acetonitrile as shown in **Figure 3.2** above. Two characteristic peaks are of interest; the aromatic C-H stretch (3000-3200 cm^{-1}) and the nitrile stretch of TCNQ (2100-2250 cm^{-1}). Initially, the TCNQ molecule has two peaks corresponding to the C-H stretch: at 3050 cm^{-1} and 3139 cm^{-1}, while the TTF molecule has peaks at 3063 cm^{-1}. Upon complexation the C-H bonds shift to 3072 cm^{-1} and 3092 cm^{-1}. Similarly, the nitrile stretch on TCNQ shifts from 2222 cm^{-1} to 2202 cm^{-1} upon formation of the CTC as seen in **Table 3.1**. Both peak shifts are in good agreement with previous literature.[53] The black CTC curve shows a decrease in % transmittance as the wavenumber decreases indicating absorption of radiation in the near IR region.

Similarly, the composite samples cooled at slow, normal, and fast speeds were analyzed by FTIR to spectroscopically confirm complexation of the CTC. **Figures 3.3 and 3.4** show above both show peak overlaps of the composite samples at 3072 cm^{-1} and 3092 cm^{-1} for the C-H stretch as well as 2202 cm^{-1} with the CTC crystallized from acetonitrile indicating the CTC forms in all three processing scenarios. As seen in **Figure 3.3** the peak signal intensity appears to decrease as the particle size increases (no crystallites vs. needle vs. dendrite) showing that increasing aggregation of the CTC micro-crystallites again leads to a decrease in light transmitted through the sample.

In polymer composites, the interfacial interaction between the filler particle and polymer matrix have the potential to affect crystallization of the matrix. In order to determine the effect of the CTC inclusion on the LDPE morphology, DSC was performed to compare the % crystallinity. As seen in **Figure 3.5** below there is no change in crystallinity observed when comparing the neat LDPE control samples to the 0.25 wt. %

CTC composite samples cooled at identical rates, however, there is a slight increase in crystallinity depending on the cooling speed. As seen in **Table 3.2** the % crystallinity as determined by DSC is between 40-45 % for all LDPE samples and shows good repeatability. The quench cooled samples have % crystallinities of ~41.4 %, the normal cooled samples are ~42.3% crystalline, and the slow cooled samples are ~44.6% crystalline. The increasing % crystallinity with decreasing cooling rate is expected as the more time the LDPE chains have to align and the higher % crystallinity is obtained.

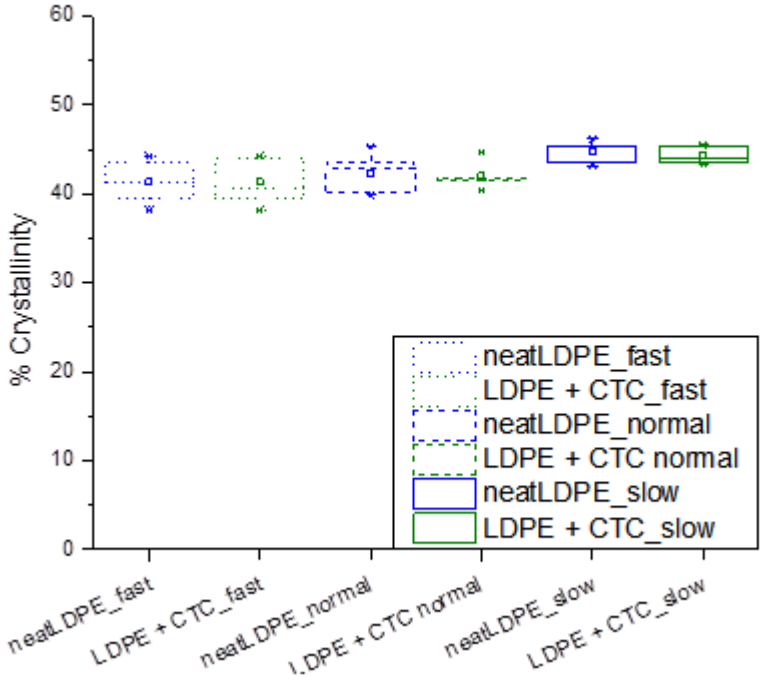

Figure 3.5: % crystallinity as a function of cooling rate, side-by-side comparison of the neat LDPE samples with the composite samples.

Table 3.2: Data comparison via DSC curves for % crystallinity analysis.

	Melting onset	melting peak	enthalpy	% crystallinity	
	°C	°C	J/g	%	std. dev
neatLDPE_fast	100.8	109.4	121.2	41.4	2.6
LDPE+CTC_fast	100.7	110.2	121.1	41.3	2.7
neatLDPE_normal	100.8	110.0	124.1	42.4	2.3
LDPE+CTC_normal	101.6	110.0	123.2	42.1	1.6
neatLDPE_slow	101.5	111.1	131.2	44.8	1.3
LDPE+CTC_slow	100.1	111.0	130.0	44.4	1.0

X-ray diffraction was used in conjunction with DSC to analyze the effect of the CTC on the morphology of the LDPE. In **Figure 3.6** below showing a representative XRD diffraction pattern displaying normalized intensity vs. 2-theta of the neatLDPE_slow and LDPE_CTC_slow. Typical of unoriented polyethylene, two sharp peaks corresponding to the crystallographic directions (110) and (200) are observed which show up as concentric Debye-Scherrer rings as seen in **Figure 3.7** as well as a broad peak corresponding to the amorphous region. Additionally, for all three pairs of control LDPE and composite LDPE with the CTC inclusions, the patterns overlap almost completely indicating that the CTC likely had no effect on LDPE crystallinity.

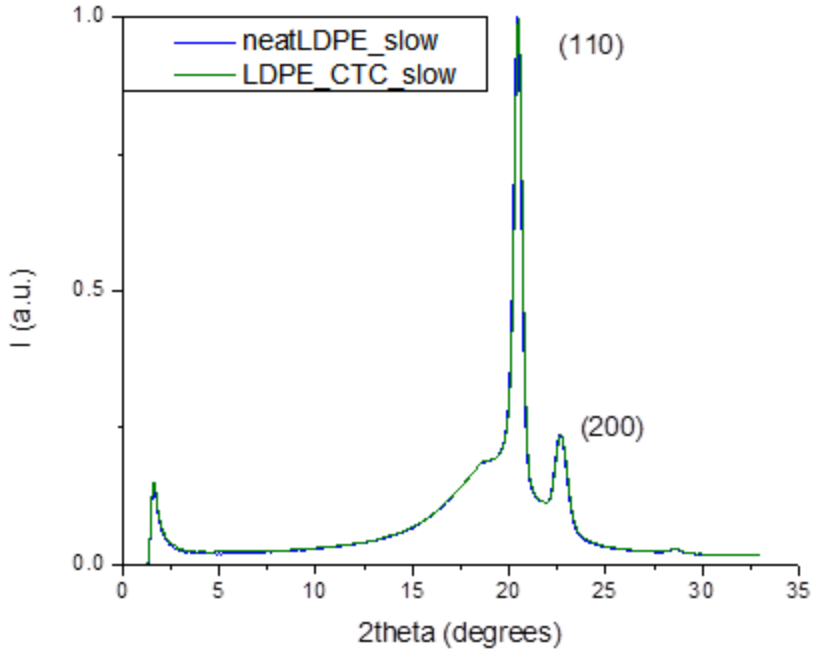

Figure 3.6: Representative XRD pattern of LDPE_CTC_slow overlayed with the neatLDPE_slow.

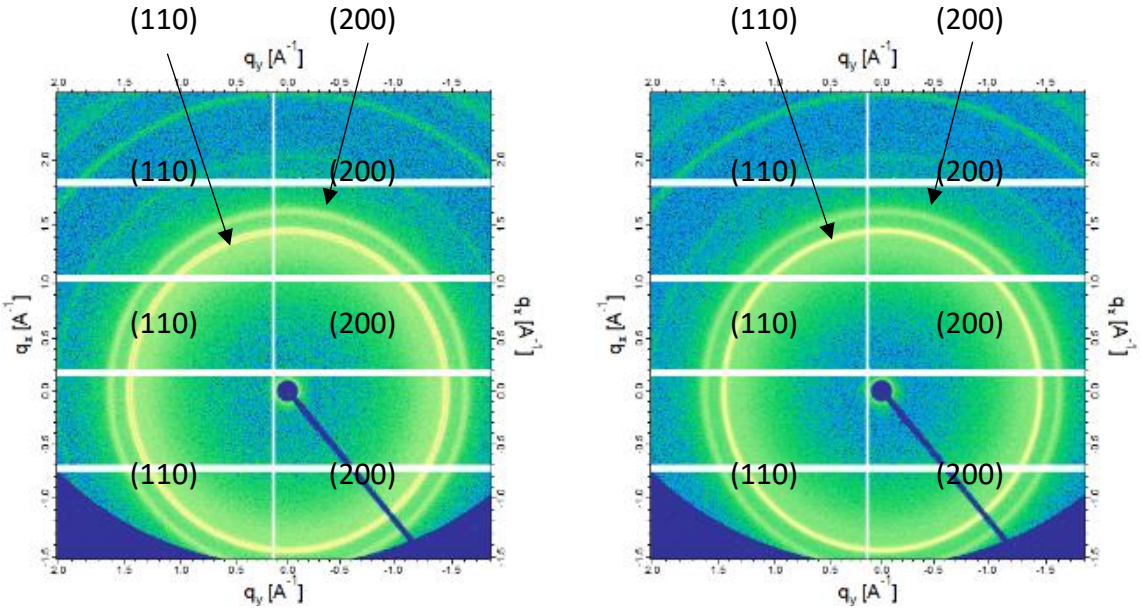

Figure 3.7: Debye-Scherrer image of LDPE_CTC_slow (left) and neatLDPE_slow (right).

In order to confirm, the % crystallinity of the samples were calculated via the 2-phase model described previously and seen in **Table 3.3**. **Figure 3.8** shows a plot of the % crystallinity for each sample, although the values determined by XRD are slightly lower than via DSC they follow the same general trend. There is no apparent difference in LDPE crystallinity upon inclusion of the CTC, similarly there is a slight increase in the crystallinity as the cooling rate decreases as expected.

Table 3.3: Peak areas of the crystalline and amorphous regions as determined by a gaussian fit function, % crystallinity as determined by XRD.

	110	200	amorphous	%
neatLDPE_fast	0.446	0.120	1.119	33.6
LDPE_CTC_fast	0.442	0.117	1.082	34.1
neatLDPE_normal	0.446	0.111	1.085	33.9
LDPE_CTC_normal	0.444	0.116	1.088	34.0
neatLDPE_slow	0.431	0.116	0.952	36.5
LDPE_CTC_slow	0.430	0.115	0.949	36.5

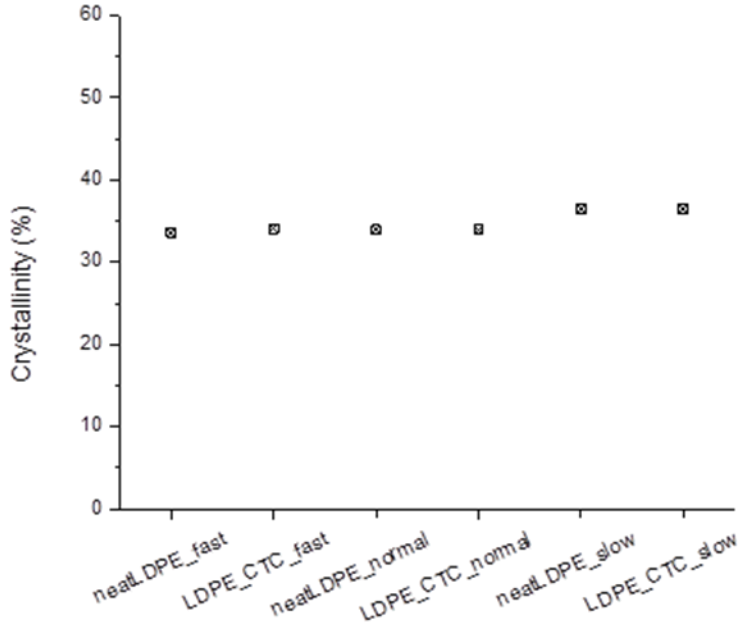

Figure 3.8: % Crystallinity determined by XRD as a function of cooling rate, side-by-side comparison of neat LDPE samples with CTC incorporated composite samples.

Next, even though the overall degree of crystallinity was unaffected, XRD was also used to qualitatively compare the LDPE crystallite dimensions to see if the crystallite size was affected. The FWHM and Bragg angle were determined for each of (110) and (200) crystallographic planes and from that the crystallite dimensions were calculated via the Scherrer equation as described in Chapter 2 and shown in **Tables 3.4** and **3.5**.

Table 3.4: Crystallite dimension of (110) plane determined by FWHM and Bragg angle.

	FWHM (theta)	rad	Bragg angle	cos(Bragg angle)	110 dimension (Å)
neatLDPE_fast	0.530	0.009	10.215	0.984	150.4
LDPE_CTC_fast	0.524	0.009	10.240	0.984	152.2
neatLDPE_normal	0.528	0.009	10.240	0.984	151.2
LDPE_CTC_normal	0.527	0.009	10.240	0.984	151.5
neatLDPE_slow	0.496	0.009	10.240	0.984	160.8
LDPE_CTC_slow	0.496	0.009	10.215	0.984	160.8

Table 3.5: Crystallite dimension of (200) plane determined by FWHM and Bragg angle.

	FWHM (theta)	rad	Bragg angle	cos(Bragg angle)	200 dimension (Å)
neatLDPE_fast	0.738	0.013	11.309	0.981	108.5
LDPE_CTC_fast	0.725	0.013	11.309	0.981	110.4
neatLDPE_normal	0.728	0.013	11.309	0.981	110.1
LDPE_CTC_normal	0.730	0.013	11.309	0.981	109.8
neatLDPE_slow	0.696	0.012	11.309	0.981	115.1
LDPE_CTC_slow	0.691	0.012	11.336	0.981	115.9

The presence of the CTC inclusion does not appear to have any influence on the crystallite sizes even with the highly branched dendritic samples as seen in **Figure 3.9**. There is a slight increase in the crystallite size as the cooling rate decreases and as expected and since the Scherrer equation gives an inverse dependence on the peak intensity the (110) crystal planes are larger than that of the (200) direction. The XRD and DSC data together indicate the LDPE crystallinity is unaffected by the presence of the CTC inclusion despite the assumedly higher interfacial area of the highly branched dendritic crystallites. This indicates that the CTC does not act as a nucleating agent for LDPE crystallization.

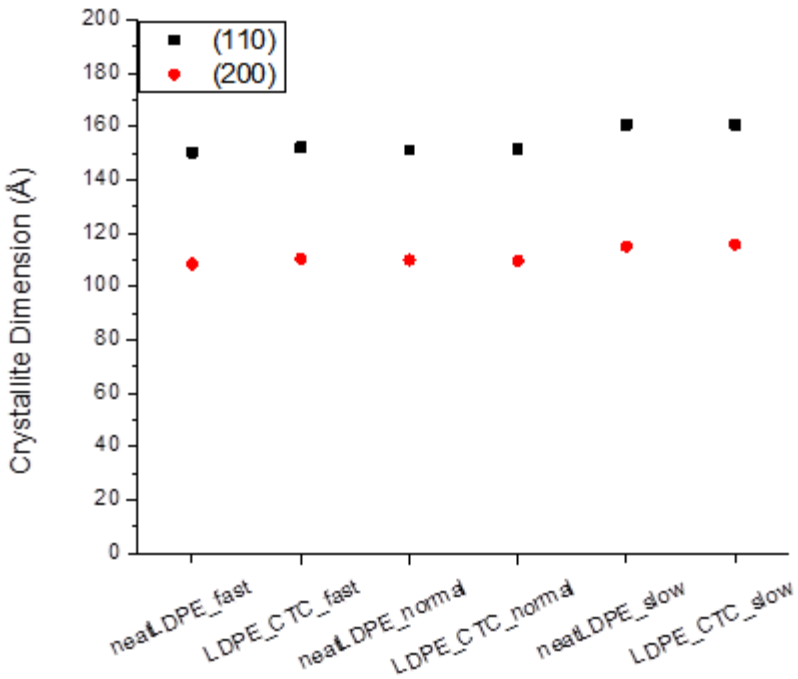

Figure 3.9: Crystallite dimension (Å) of the (110) and (200) crystallographic planes.

Tensile testing was performed on an average of 5 samples to understand the impact of the CTC morphology on the composite mechanical properties. **Figure 3.10** compares the Youngs modulus of each sample giving an indication of its stiffness as determined by the slope in the linear region of the stress-strain curve. For the composite samples, the quench cooled sample has the lowest Youngs moduli of approximately ~80 MPa, increasing to ~90 MPa when cooled normally, and finally ~123 MPa for the slowly cooled dendritic samples. However, when comparing against the control samples without the presence of the CTC there is no apparent change in the moduli and interestingly a small increase of ~90 MPa to ~96 MPa when removing the CTC. This indicates that the presence of the CTC as either a needle or dendritic particle inclusion likely doesn't affect the stiffness of the composite and potentially decreases the mechanical properties. In

Figure 3.11 below, the yield stress increases from ~11 MPa with no CTC micro-crystallites to ~11.7 MPa with 'needle' crystallites and finally ~14 MPa for the dendritic crystallites however in agreement with the Youngs' moduli trend there is no substantial difference in comparison with the control samples indicating the cooling rate and not the CTC morphology is more important to the mechanical properties. The tensile strength as shown in **Figure 3.12** below, the fast-cooled samples have a peak stress of ~11 MPa, the normal cooled composites have a maximum strength of ~12.2 MPa, and the slow cooled samples again have the highest peak stress of ~13.8 MPa, again however the neat LDPE samples are in the same vicinity as their composite counterparts. Lastly in **Figure 3.13** is a plot of the strain at break, no apparent trend could be discerned as the repeatability was poor. However, the slow-cooled composite samples with dendritic CTC inclusions failed at considerably lower strains in comparison to the other samples.

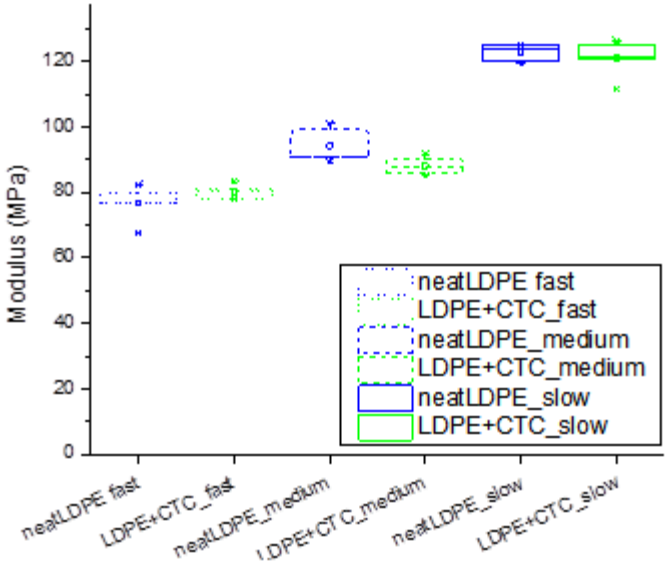

Figure 3.10: Young's Modulus as a function of cooling rate, side-by-side comparison of neat LDPE samples and CTC LDPE composites.

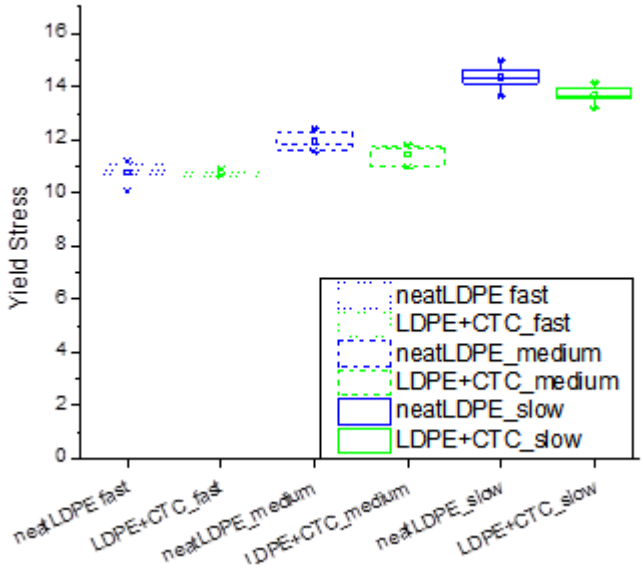

Figure 3.11: Yield Stress as a function of cooling rate, side-by-side comparison of neat LDPE samples and CTC LDPE composites.

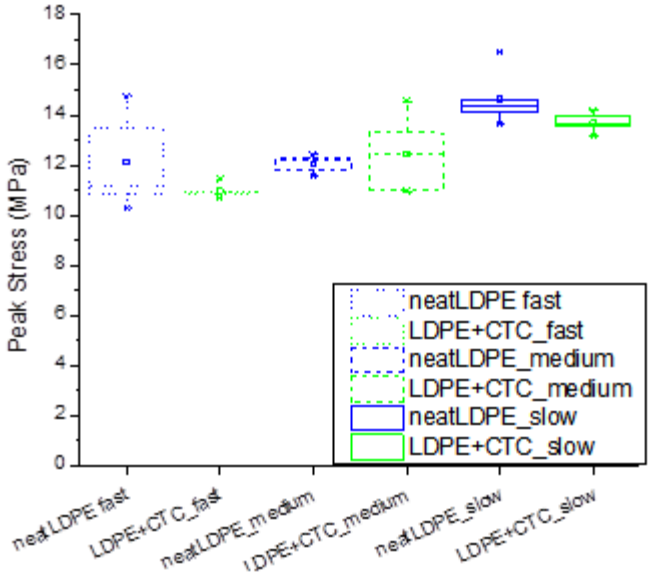

Figure 3.12: Maximum Strength as a function of cooling rate, side-by-side comparison of neat LDPE samples and CTC LDPE composites.

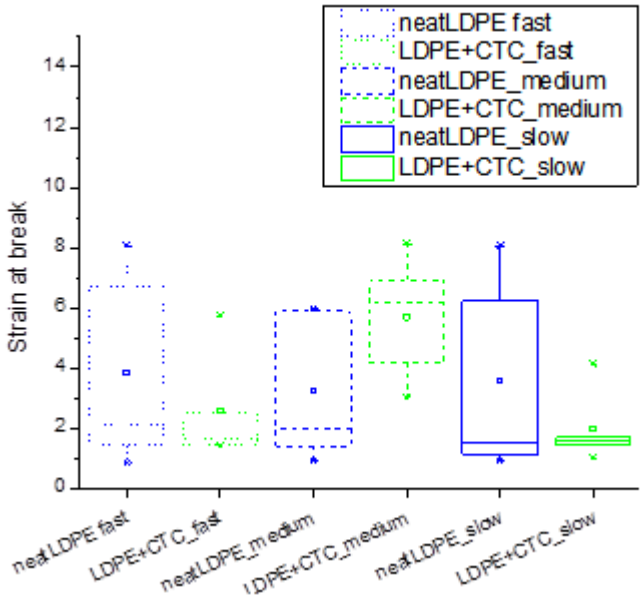

Figure 3.13: Strain at break as a function of cooling rate, side-by-side comparison of neat LDPE samples and CTC LDPE composites.

Next, in order to see whether the size of the dendrite particles had an effect on the composite mechanical properties the dendrite particle size was varied either by increasing or decreasing the compression-molding temperature by ± 5 °C or finally by increasing the wt. % CTC to 0.30 and slowly cooling from 190 °C which were the conditions found to create the largest dendrite particles as seen below in **Figure 3.14**. As seen on the right-most sample in **Figure 3.14**, the large dendrite particles were inhomogeneously spread throughout the sample potentially as a result from differences in the sample location in relation to the heating element, and thus only specimens with the large dendrites dispersed throughout the center region were used for further analysis. All samples were slowly cooled on the melt press from the designated temperature in order to form dendritic CTC morphologies. However, pressing and cooling from temperatures exceeding 190 °C did not form larger dendrites but caused the CTC to precipitate out of the sample prematurely (not shown). Additionally, as seen in **Figure 3.14** the sample color changes with increasing dendrite particle size from a dark brown with fine speckles at 165 °C, to a medium brown at 170 °C, and a light brown at 175 °C showing an increase in the aggregation of the dendritic CTC particles.

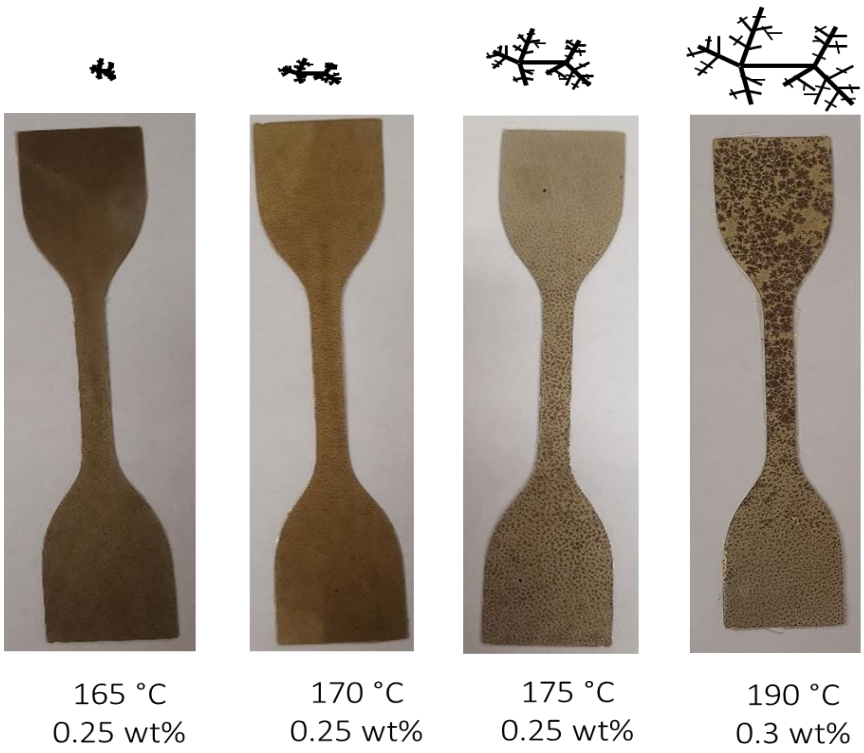

Figure 3.14: Photograph of tensile bars showing visualization of increasing dendrite particle size from left to right.

Tensile testing was performed on the samples in an identical manner as before. **Figures 3.15, 3.16**, and **3.17** show plots of the Youngs moduli, Yield stress, and maximum stress respectively. There is no difference in the properties based on the particle size and the values are in good agreement with the slow cooled samples analyzed previously. In **Figure 3.18**, however there is a decrease in the strain at break as the dendrite particle size increases indicating the dendrites have a deteriorating effect on the mechanical properties and potentially influence the failure mechanism of the composite.

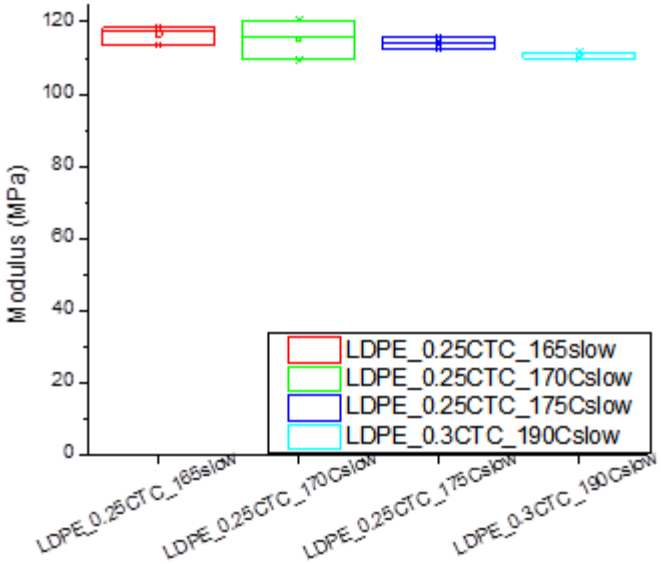

Figure 3.15: Youngs Modulus as a function of dendrite particle size.

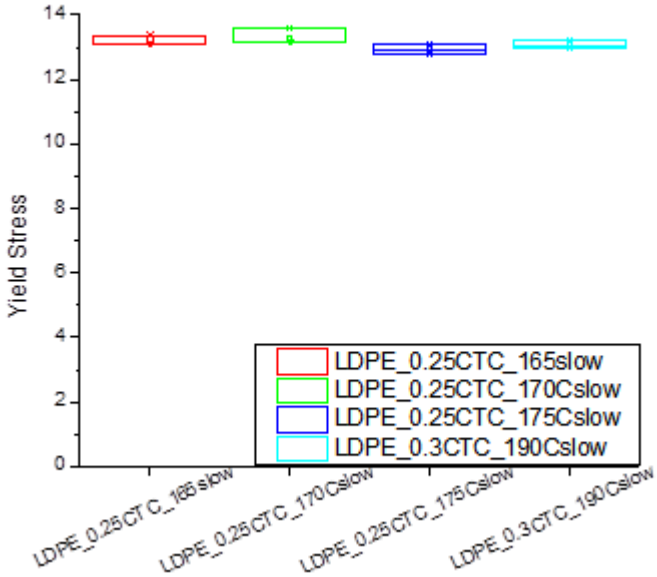

Figure 3.16: Yield Stress as a function of dendrite particle size.

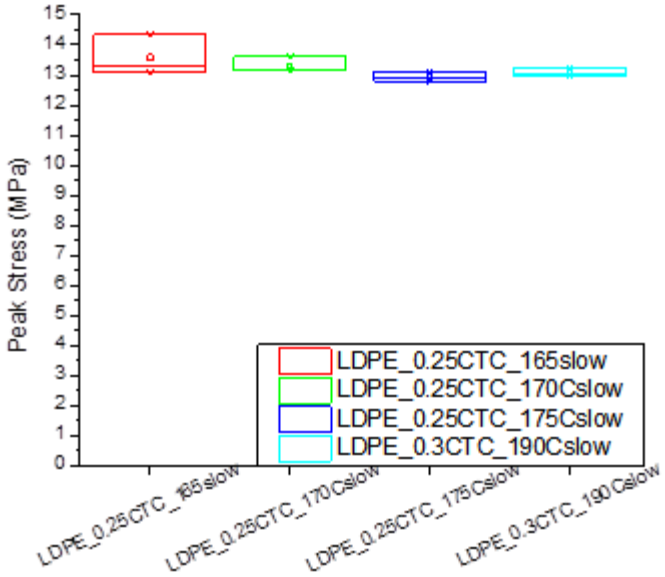

Figure 3.17: Maximum strength as a function of dendrite particle size.

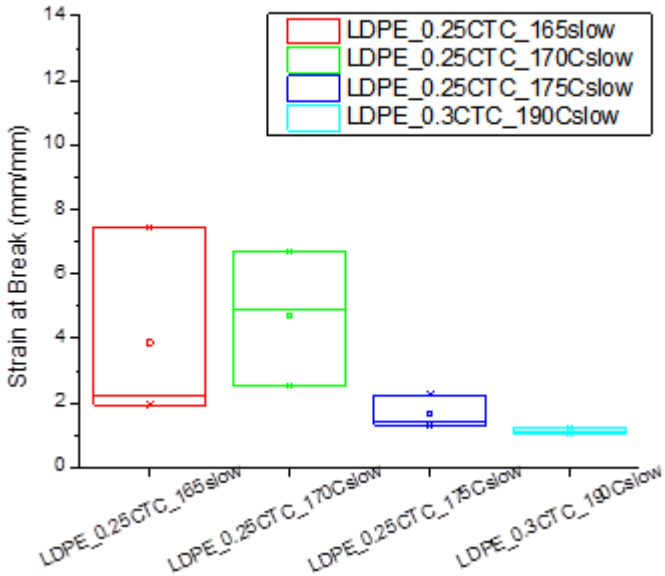

Figure 3.18: Strain at break as a function of dendrite particle size.

Lastly, a new grade of LDPE (DOW LDPE 132I) without an anti-blocking agent was obtained to eliminate the interaction of the polymer matrix and the CTC with talc powder additive. Additionally, one of the disadvantages of forming dendritic CTC morphologies is the slow cooling time which can often exceed an hour. As seen in **Figure 3.19** below, it was observed that by holding the compression-molding temperature consistent at 180 °C and normal cooling them on the countertop the morphology could be gradually changed from small needle microcrystals (**Figure 3.19e** and **3.19f**) to underdeveloped dendrites (**Figure 3.19c** and **3.19d**) and finally large dendrites (**Figure 3.19b**) by changing the concentration of the CTC only from (0.16 – 1 wt. %). Lastly, if the concentration of CTC was low enough, as seen in the 0.16 wt. % sample, essentially no micro-crystallites were observed.

The CTC particle dimensions were characterized via ImageJ as summarized in **Tables 3.6, 3.7**, and **3.8** below. In **Table 3.6**, by decreasing the CTC concentration from 1 wt. % to 0.85 wt. % the length of the needle like particles increases from 17.4 ± 2.1 μm to 39.7 ± 8.4 μm. Similarly, in **Table 3.7**, the longest diameter of the dendrite particles increases from 82.6 ± 15.3 μm to ~443.9 ± 124.0 μm upon further decreasing the concentration from 0.6 wt. % to 0.3 wt. % indicating that as the concentration decreases the number of seed crystals decrease and results in larger crystal growth. This is also seen in **Table 3.8**, where the particle number density decreases with decreasing concentration and results in particles of larger average size. Lastly, **Table 3.8** also shows that the

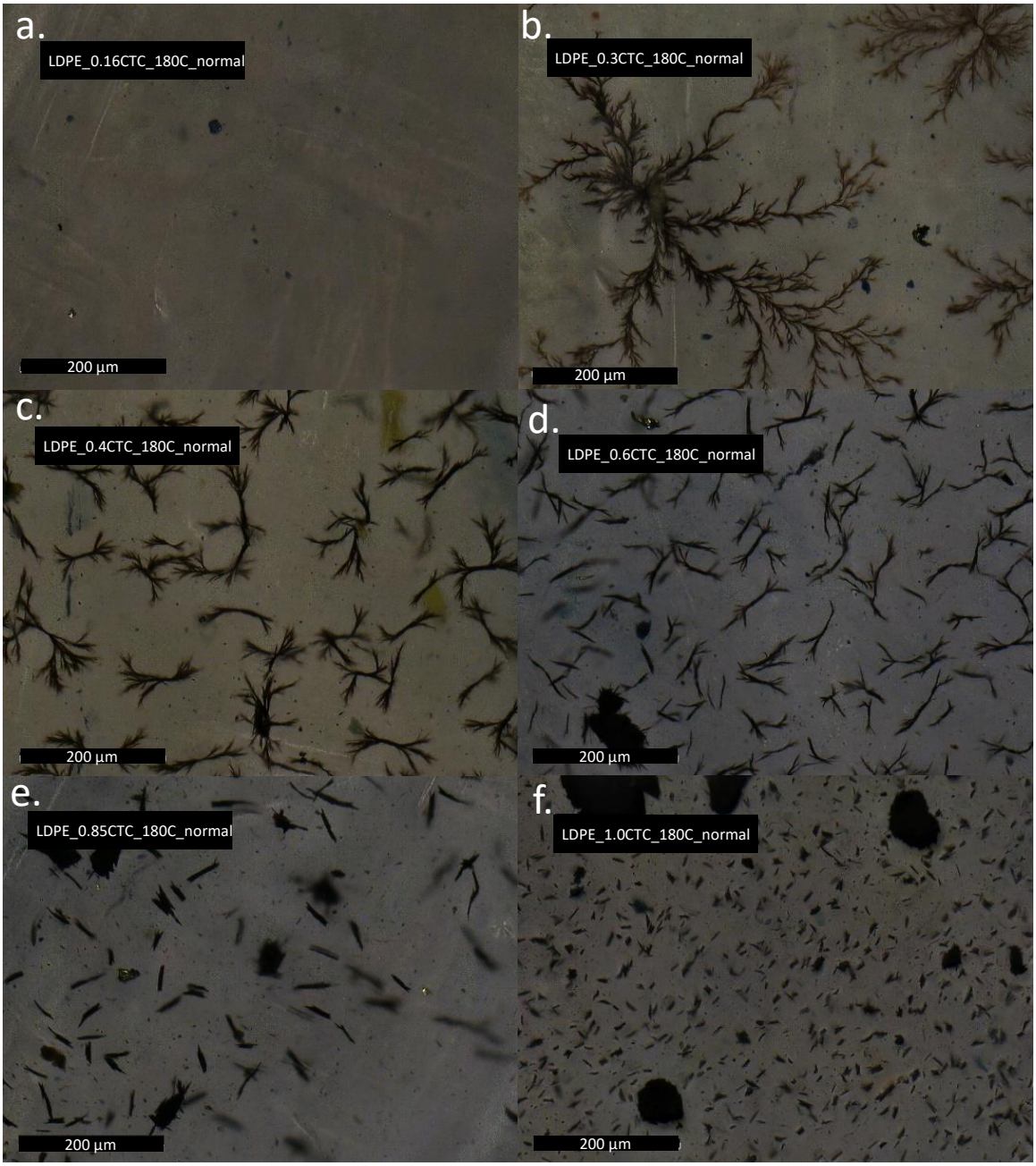

Figure 3.19: Optical micrographs of LDPE composites that were normal cooled from 180 °C with varying CTC concentration a.) 0.16 wt. % CTC, b.) 0.30 wt. % CTC, c.) 0.40 wt. % CTC, d.) 0.60 wt. % CTC, e.) 0.85 wt. % CTC, and f.) 1.0 wt. % CTC.

dendrite morphologies have comparatively higher surface areas as estimated via the 2D-surface area fraction assumedly due to their highly branched nature.

Table 3.6: Needle length and width calculation for the 1 wt. % CTC and 0.85 wt. % CTC.

CTC wt. %	1		0.85	
	length (μm)	width (μm)	length (μm)	width (μm)
Average	17.4	3.1	39.7	5.4
STDEV	±2.1	±1.4	±8.4	±1.3

Table 3.7: Longest end-to-end distance and radius of the dendritic CTC particles.

CTC wt. %	0.6		0.4		0.3		0.16	
	diameter (μm)	radius (μm)	diameter (μm)	radius (μm)	diameter (μm)	radius (μm)		
Average	82.6	44.6	109.2	58.2	443.9	271.8	N/A	N/A
STDEV	±15.3	±9.6	±26.5	±13.6	±124.0	±92.3	N/A	N/A

Table 3.8: Average particle size, 2D surface area fraction, and 2D particle number density as determined via ImageJ.

CTC wt. %	1	0.85	0.6	0.4	0.3	0.16
avg. size (μm^2)	66.8	336.5	480.3	2210.9	11979	N/A
2D Surface Area fraction (%)	9.90	9.87	12.18	14.97	15.69	N/A
2D number density (particles / mm^2)	1488.00	293.30	253.50	67.76	11.94	N/A

The TTF and TCNQ complexation was spectroscopically confirmed as before via FTIR as seen in **Figure 3.20** below. Specifically looking at the presence of the nitrile peak of TCNQ at 2202 cm^{-1} and disappearance of the peak at 2222 cm^{-1}. In general, as the

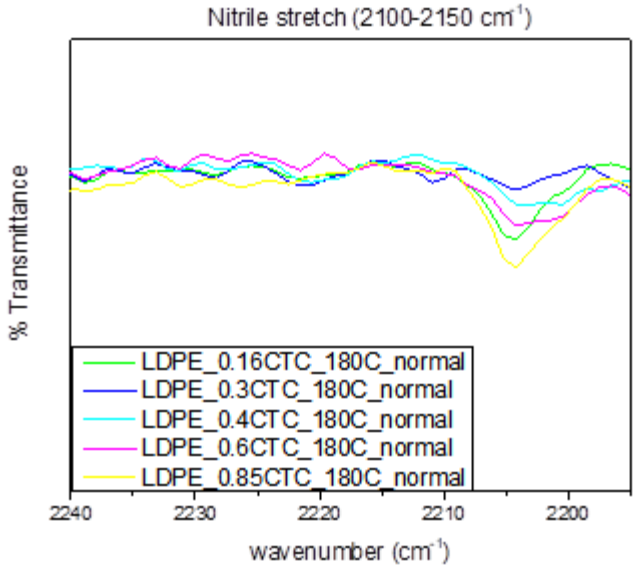

Figure 3.20: Overlay of FTIR spectra showing nitrile stretch of the different LDPE +CTC composites.

particle size increased the peak intensity decreased indicating a higher degree of aggregation in the system.

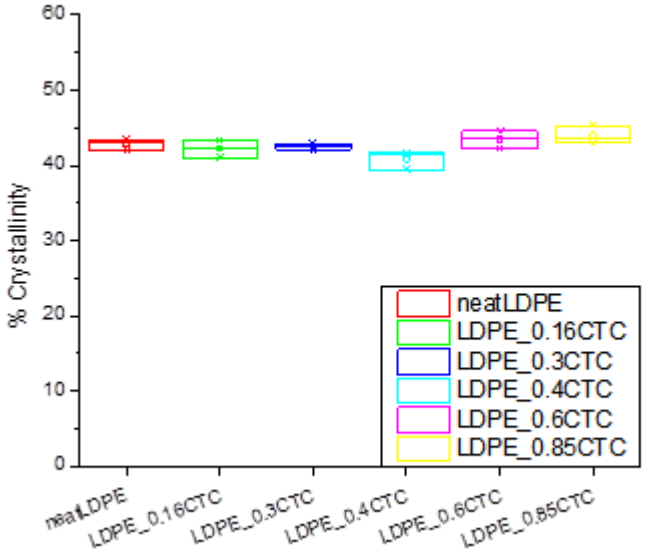

Figure 3.21: Plot showing % crystallinity as a function of CTC concentration (0.16 – 0.85 wt. %) of LDPE composite samples all cooled normally from 180 °C.

Similarly, the % crystallinity was also determined via DSC as seen in **Figure 3.21** and **Table 3.9** below. For all of the samples, the degree of crystallinity was determined to be approximately ~41-43% and is independent of the concentration of CTC present. This agrees with the results above that the presence of the CTC particle does not affect LDPE crystallization irrespective of CTC morphology. Similarly, since the rate of cooling was held constant in this set of samples, any change in mechanical properties can be attributed to differences in the CTC concentration/morphology and not LDPE crystallinity.

Table 3.9: Data table of calculated % crystallinity determined by DSC as a function of CTC concentration.

	melting onset °C	melting peak °C	enthalpy J/g	% crystallization %	St. dev.
neatLDPE	101.0	109.8	125.6	42.9	0.7
LDPE_0.16CTC	98.6	110.9	123.8	42.2	1.2
LDPE_0.3CTC	101.6	110.8	124.5	42.5	0.4
LDPE_0.4CTC	101.7	111.5	119.7	40.9	1.3
LDPE_0.6CTC	104.2	110.8	127.3	43.4	1.1
LDPE_0.85CTC	104.8	111.5	128.8	44.0	1.2

Tensile specimens were prepared as seen in **Figure 3.22** below. The neat LDPE sample appeared a transparent clear color, the 0.16 wt. % CTC composite sample appeared as a transparent light green color, the three dendritic samples 0.3 wt. % - 0.6 wt. % had a speckled pattern and were shades of brown. The 0.85 wt. % CTC composite sample with needle particles appeared very dark brown in color. **Figure 3.23** below is a plot comparing the average Youngs moduli for each sample, the neat LDPE has a modulus of ~75 MPa which interestingly decreases to ~60 MPa for the 0.16 wt. % CTC composite sample and potentially indicates a plasticizing effect when CTC crystallization is minimal. The modulus shows an increase from ~75 MPa to ~95 MPa as the CTC

concentration increases toward 0.85 wt. % despite the decrease in estimated 2D surface area fraction. Similarly, in **Figure 3.24** below, the yield stress gradually increases from ~10.8 MPa to ~12 MPa with a slight decrease for the 0.16 wt. % CTC sample. The maximum strength decreased as a function of CTC concentration as seen below in **Figure 3.25** which is likely an artifact of the decrease in strain at break trend seen in **Figure 3.26** and **3.27**.

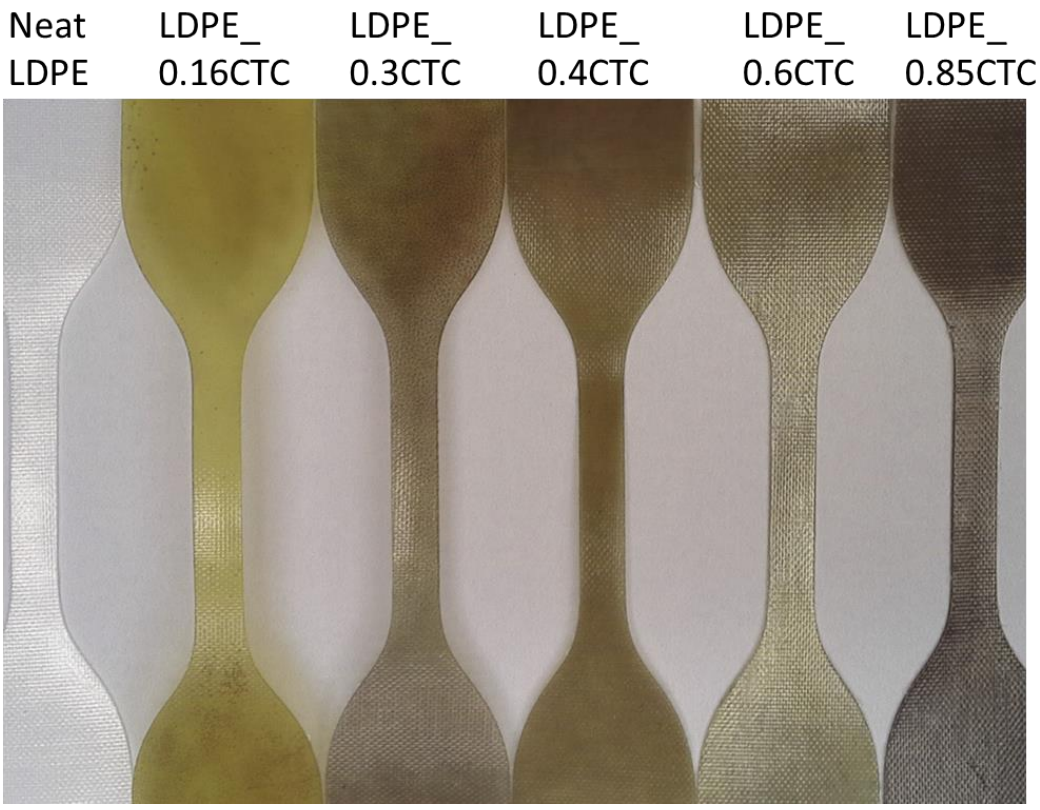

Figure 3.22: Photograph showing tensile specimen of the control LDPE and the five composite samples under analysis.

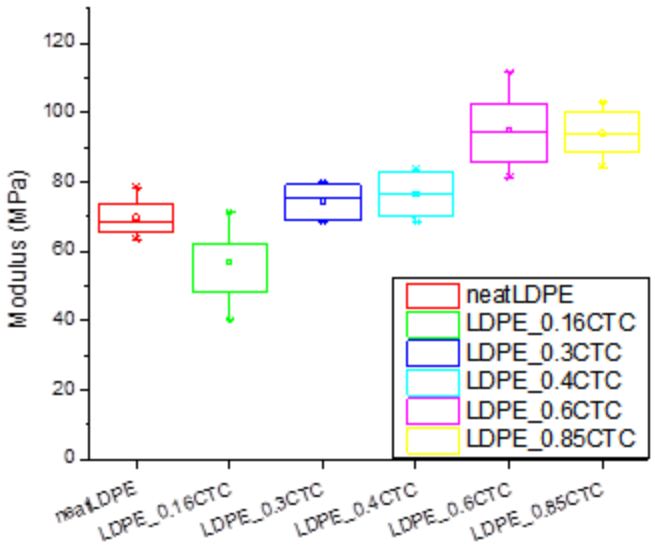

Figure 3.23: Plot showing modulus as a function of CTC concentration.

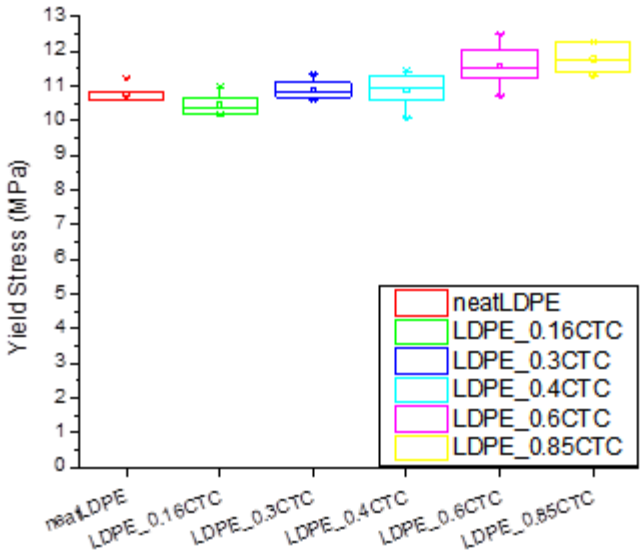

Figure 3.24: Plot of yield stress as a function of CTC concentration.

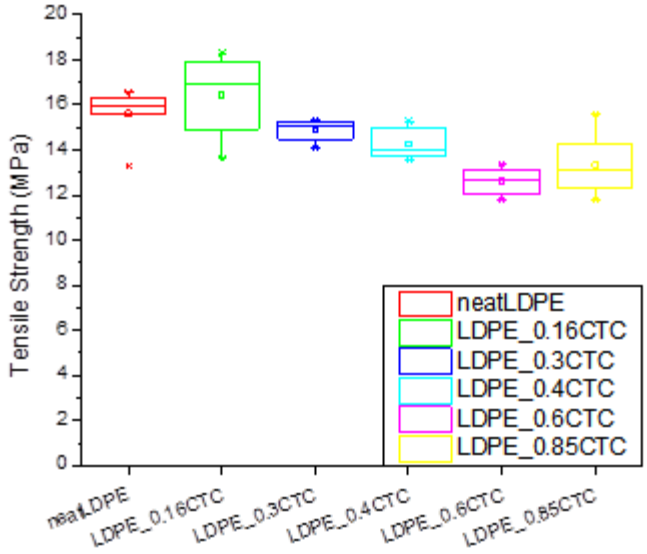

Figure 3.25: Plot showing the maximum tensile strength of each sample as a function of CTC concentration.

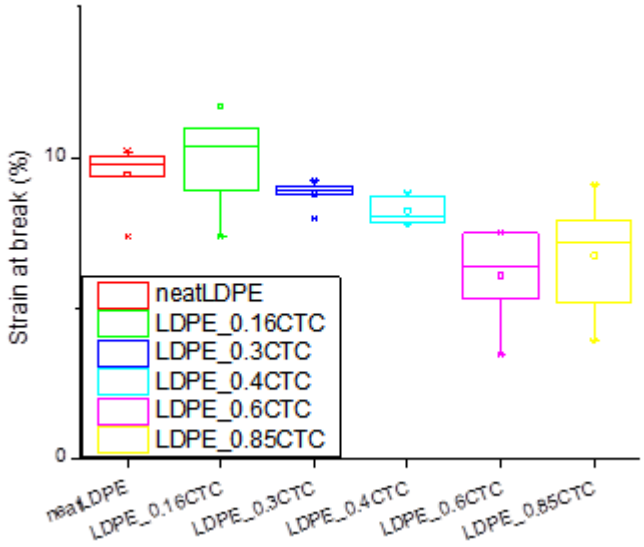

Figure 3.26: Plot of strain at break with increasing CTC concentration.

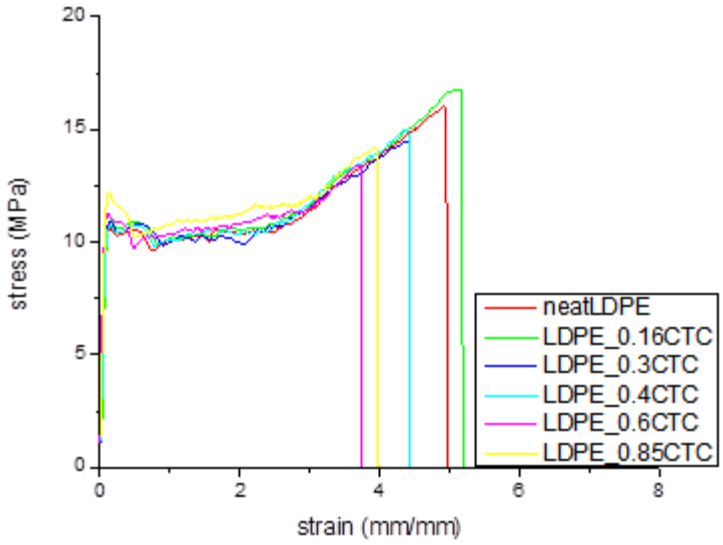

Figure 3.27: Representative stress-strain curves overlayed for each composite sample normal cooled from 180 °C.

CHAPTER IV – CONCLUSION

The morphology of charge-transfer complexes based on TTF-TCNQ were successfully formed *in situ* in LDPE matrices using a compression-molding process. The architecture (needles or dendrites) and sizes were able to be selectively tuned by controlling the CTC concentration, compression-molding temperature, or cooling rate. Based on the initial temperature vs. concentration screening study there is an optimal CTC concentration range (~0.25 wt. %) for dendrite growth; at concentrations below 0.25 wt. % crystal growth is poor potentially indicating the collision frequency of the CTC molecules is too low. Additionally, at concentration above 0.85 wt. % no dendrite formation occurred indicating the secondary crystallization necessary to form branches is unfavored. Similarly, for samples cooled from temperatures below 160 °C no dendrite formation occurred indicating the LDPE viscosity was too high for diffusion-limited growth to occur at a reasonable rate. Similarly, in the experiment shown in ***Figure 3.19*** above; when the temperature and cooling rate are held constant the CTC micro-crystallite morphology can be selectively tuned from needle-like crystals at higher concentrations (0.85 and 1 wt.%) to poorly developed dendrites at intermediate concentrations (0.4 and 0.6 wt. %) to highly branched dendrites (0.25 and 0.3 wt. %) however again at 0.16 wt. % CTC crystal growth is no longer occurs. FTIR spectroscopy and optical imaging were used to confirm complexation of the CTC. In optical imaging the formation of a dark brownish-black particulate was observed and shifts in the aromatic C-H peaks to 3072 cm^{-1} and 3092 cm^{-1} and the nitrile stretch in TCNQ shifting from 2222 cm^{-1} to 2202 cm^{-1} in the FTIR spectra for all three cooling rates (slow, normal, and fast) confirmed complexation occurred in the composite samples.

Particle inclusions such as the TTF-TCNQ have the potential to affect LDPE crystallization due to matrix-filler interactions; LDPE is non-polar and has a lower surface energy in comparison to the polar TTF-TCNQ molecules suggesting a preference for the LDPE to wet the CTC particle surface. DSC and XRD were used to analyze the effect of the CTC on the LDPE crystallization. However, for either of the LDPE grades used, the percent crystallinity as determined by DSC was unchanged between the neat LDPE controls and the composite samples cooled at the same rate as seen in ***Figure 3.5***. Deconvoluting the XRD diffraction patterns into their amorphous and semi-crystalline regions confirmed this observation as seen in ***Figure 3.8***. XRD was further used to estimate the LDPE crystallite dimensions via the Scherrer equation as seen in ***Tables 3.4 and 3.5*** and again there was no difference observed between the control and composite samples. Based on the DSC and XRD experiments, despite the high surface-to-volume ratio of the dendritic particles and the high surface energy of the CTCs there is no apparent effect on LDPE crystallization that may affect the mechanical properties.

There were three experiments looking at the effect of the CTC inclusions on the composite mechanical properties. First, the concentration and temperature were held constant at 0.25 wt. % and 170 °C and the cooling rate was varied (fast, normal, slow). The stiffness, ultimate strength, and yield stress were unchanged upon addition of the CTC molecules indicating there was no reinforcing effect observed despite the higher surface-to-volume ratio of the dendritic micro-crystallites. There was no observed trend in the elongation at break for the quench-cooled (no micro-crystallites) and normal-cooled (needle), however for the dendritic sample (slow cooled) the samples failed at considerably lower strains in comparison to the controls as seen in ***Figure 3.13***. This

phenomenon was observed again when varying the dendrite particle size in the second experiment. The modulus, yield stress, and ultimate strength were similar at any dendrite size however the strain at break decreased as the dendrite particle size increased. This indicated that the CTC particles did not act as reinforcing agents but may contribute to the failure mechanism of the samples where the large dendritic particles introduced defects to the sample. It was theorized that talc powder used as an anti-blocking agent in the LDPE 133A could interfere with the matrix-filler interactions leading to the observed results. However, for the new LDPE grade 132I, the formation of the CTC crystallites did not follow the same concentration and temperature dependence as the 133A grade demonstrating the highly variable nature of the CTC crystallization and surprisingly was able to form dendritic CTC crystallites while normal-cooling (~3 minutes) on the countertop. In this experiment the temperature and cooling rate were held constant and the concentration of the CTC was varied to form the different particle architectures as seen in ***Figure 3.19.*** In **Figure 3.23**, the neat LDPE has a modulus of ~75 MPa which interestingly decreases to ~60 MPa for the 0.16 wt. % CTC composite sample and potentially indicates a plasticizing effect when CTC crystallization is minimal. However, the modulus then shows an increase from ~75 MPa to ~95 MPa as the CTC concentration increases toward 0.85 wt. % despite the decrease in estimated 2D surface area fraction going from dendritic to needle-like crystals which was not expected. It was initially hypothesized that the dendritic CTC particles would enhance the composites mechanical properties for one of two reasons: 1- the increased surface-to-volume ratio of the dendritic particles would lead to a significantly larger interphase in comparison to the needle-like crystals or 2-the highly branched nature of the dendrites would act as a rigid

particle framework for the LDPE to entangle with or create a constrained matrix resulting in a reinforcing effect. Since no reinforcing effect was observed for the dendritic samples the matrix-filler interactions are likely too poor or the dendritic CTC microcrystallites act as aggregates rather than reinforcing particles. The slight increase in modulus as a function of concentration can potentially be an artifact of the testing procedure or possibly the dense particle aggregates seen at higher concentrations (***Figure 3.19e*** and ***3.19f***), or as a result of the decrease in aggregation with decreasing particle size. The yield stress plot follows a similar trend as seen in ***Figure 3.24*** with a slight decrease for the 0.16 wt. % sample**.** However, the maximum strength decreased as a function of CTC concentration as seen in **Figure 3.25** which is likely a consequence of the decrease in strain at break trend seen in **Figure 3.26** and **3.27**. Interestingly, the strain at break decreased as a function of concentration and not the particle surface-to-volume ratio as seen previously indicating the role of the CTC on the sample failure is still not well understood.

There are various areas that may be improved upon or investigated in the future to obtain a better understanding of the effect of CTCs in polymer composites. First, the CTCs potentially do not act as reinforcing agents but as particle aggregates that result in deteriorated mechanical properties, efforts to control dispersion and interparticle spacing can be studied. Secondly, efforts to better control CTC growth as the CTC crystallization is highly variable to many factors such as slight differences in concentration, temperature, and location with respect to the heating element which may contribute to the non-uniform crystals. Third, if the LDPE and the TTF-TCNQ have poor matrix-filler interactions, other polymer matrices can be investigated for a potential better match. If DSC and XRD

are insufficient to see any effects on LDPE crystallinity, more sensitive techniques can potentially be investigated to directly measure the interphase. Lastly, research into other morphological extremes such as nanoparticle CTCs and reticulated CTCs may provide better insight into the effect of the CTC morphology on composite properties.

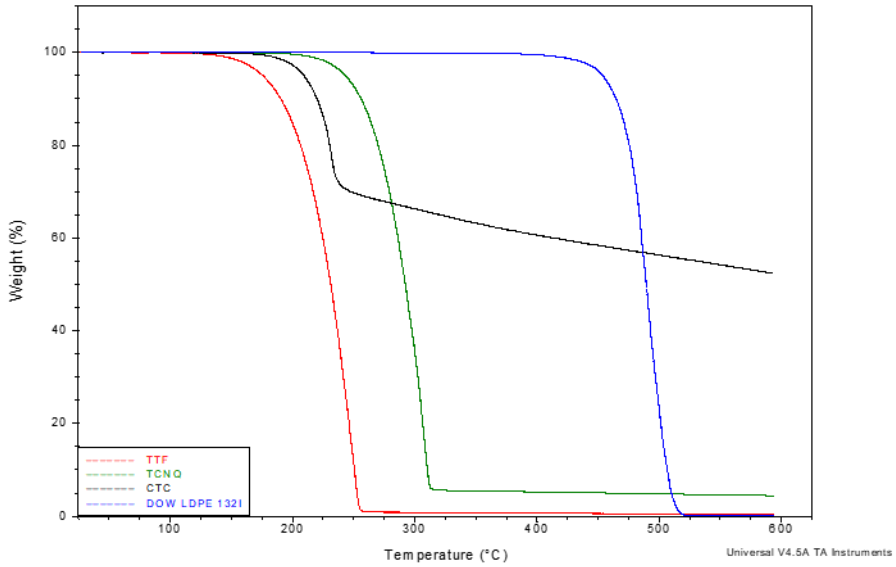

Figure A.1: TGA thermogram overlay of TTF, TCNQ, CTC, and LDPE.

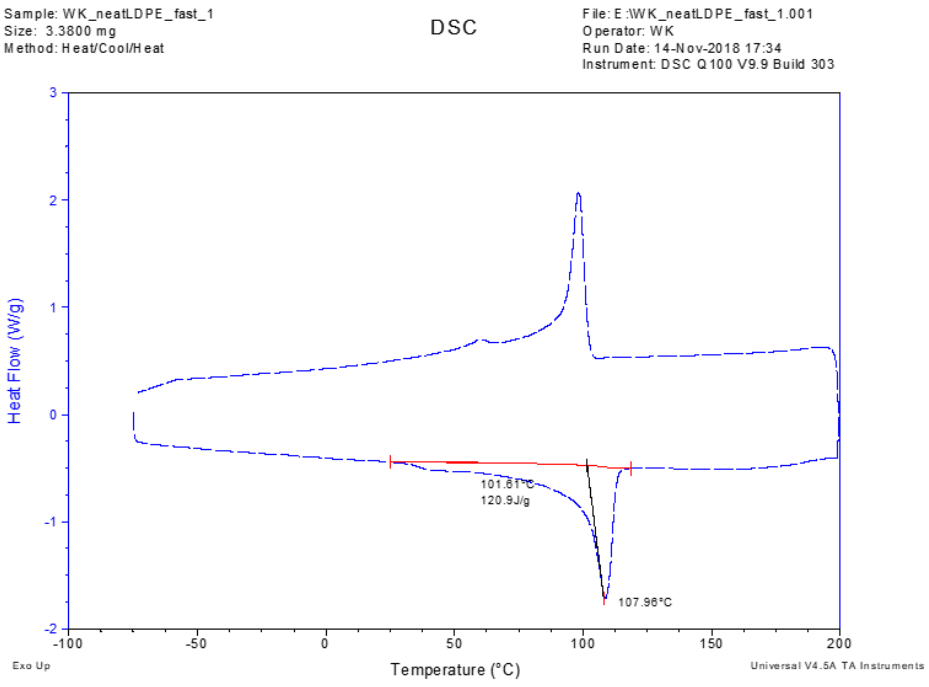

Figure A.2: Representative DSC thermogram of neatLDPE_fast.

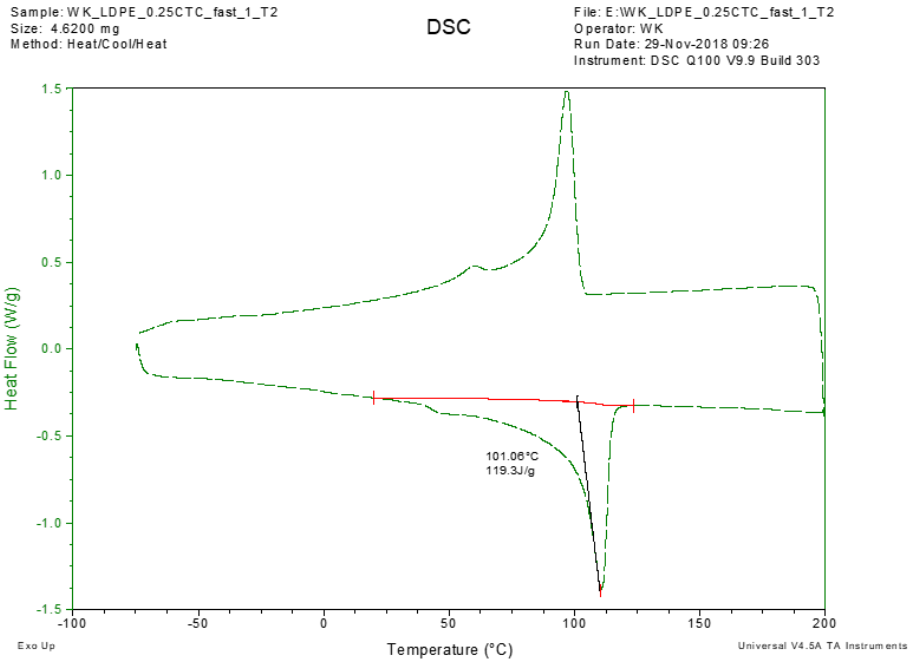

Figure A.3: Representative DSC thermogram of LDPE_CTC_fast.

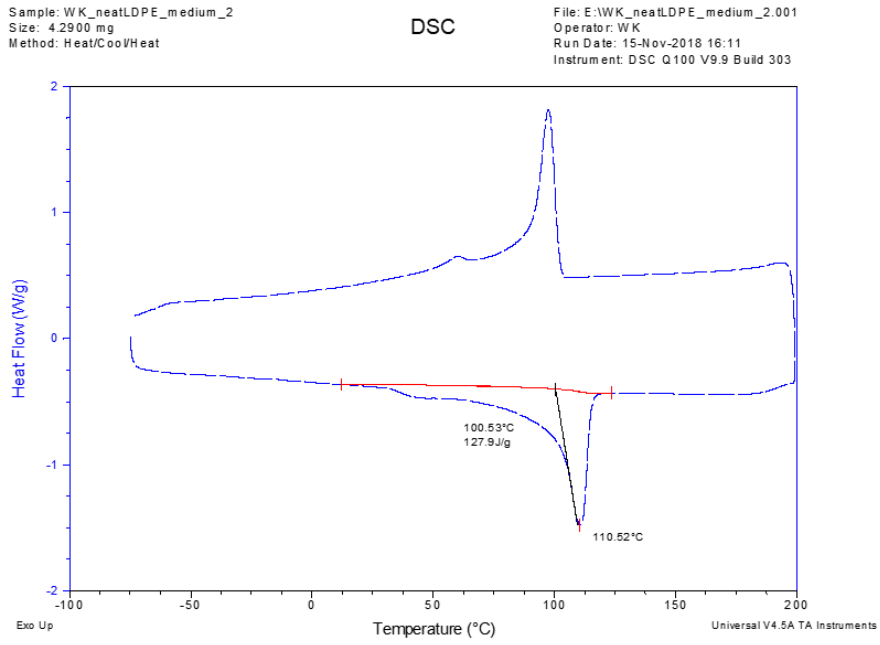

Figure A.4: Representative DSC thermogram of neatLDPE_normal.

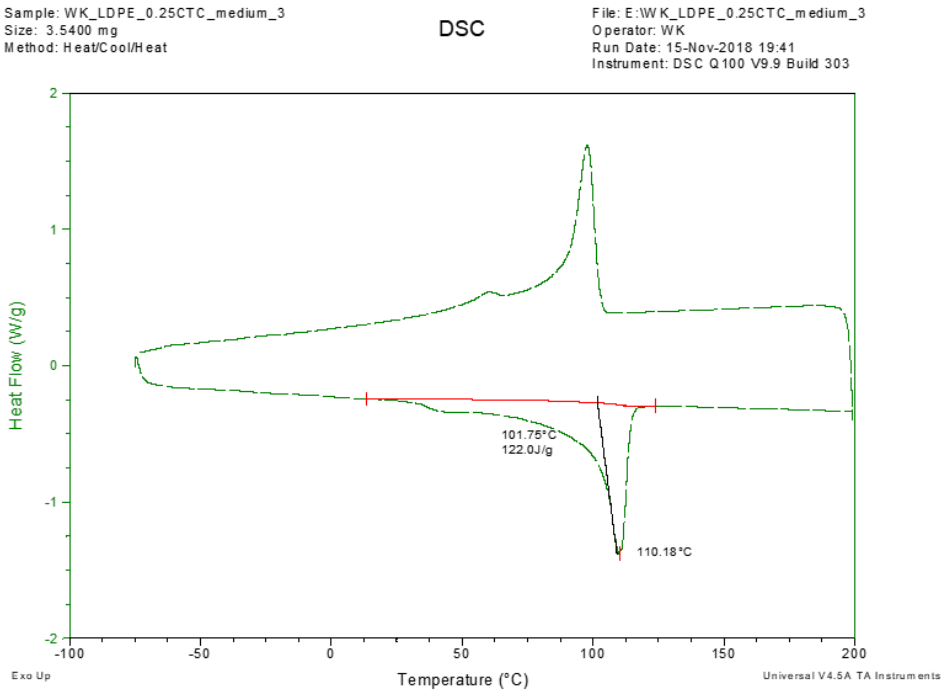

Figure A.5: Representative DSC thermogram of LDPE_CTC_normal.

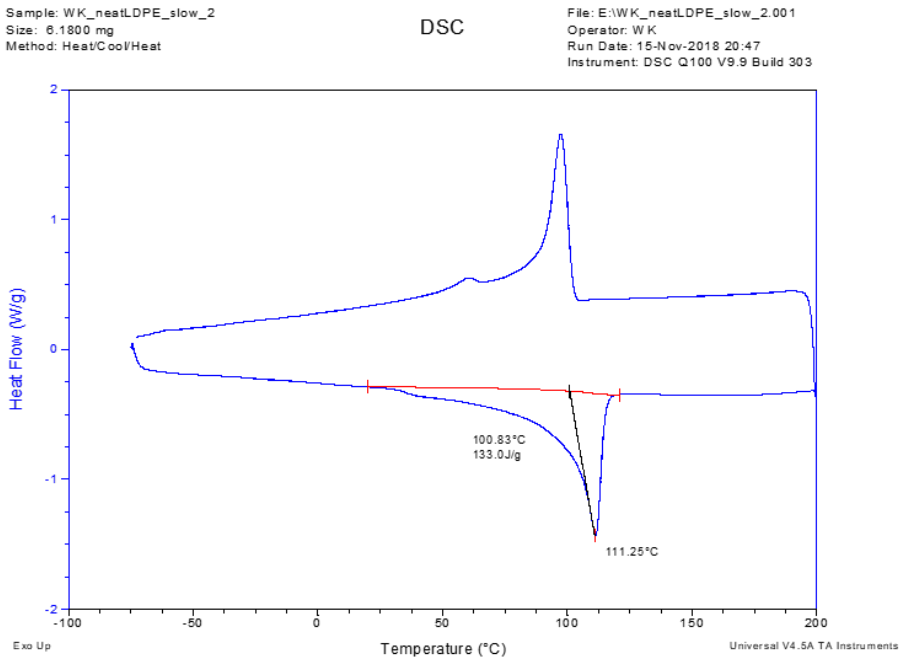

Figure A.6: Representative DSC thermogram of neatLDPE_slow.

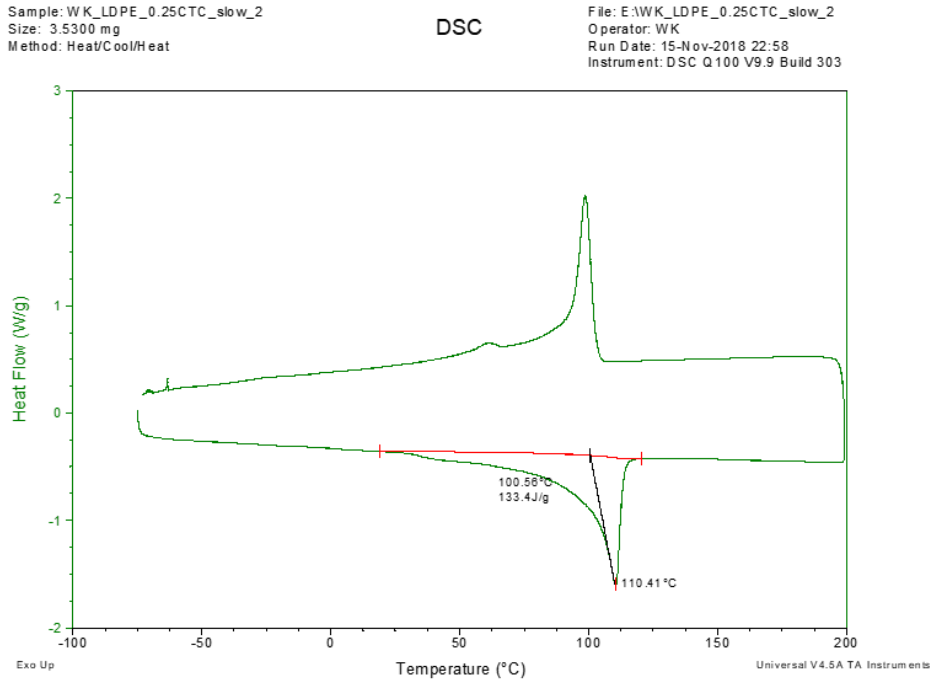

Figure A.7: Representative DSC thermogram of LDPE_CTC_slow.

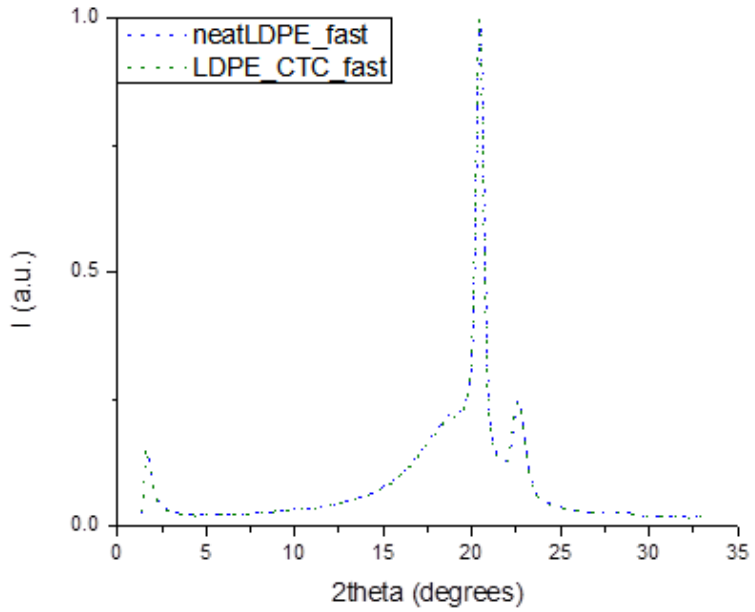

Figure A.8: XRD diffraction pattern overlay fast-cooled samples.

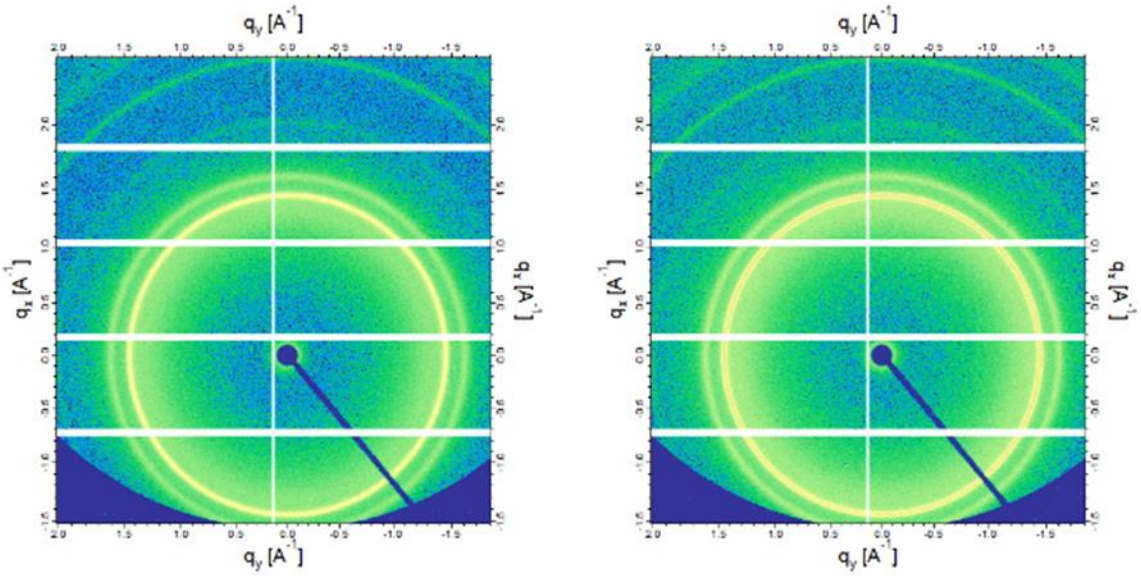

Figure A.9: Debye-Scherrer images of fast-cooled samples, neatLDPE_fast (left) and LDPE_CTC_fast (right).

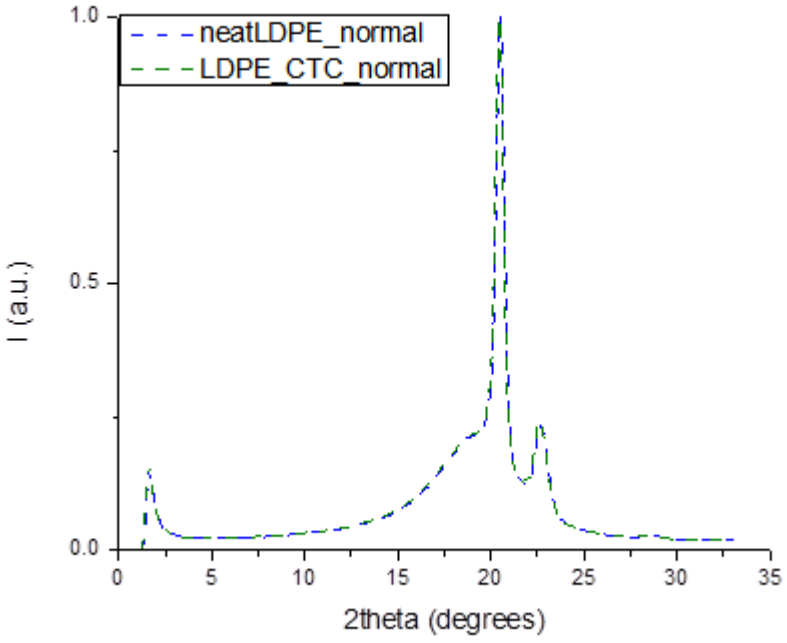

Figure A.10: XRD diffraction pattern overlay of normal-cooled samples.

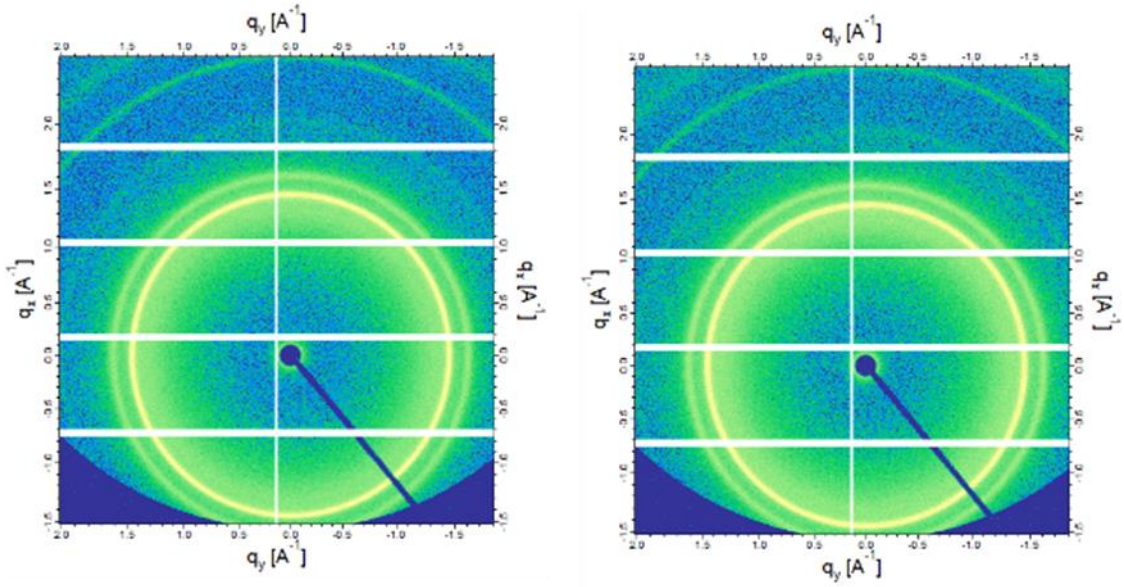

Figure A.11: Debye-Scherrer images of neatLDPE_normal (left) and LDPE_CTC_normal (right).

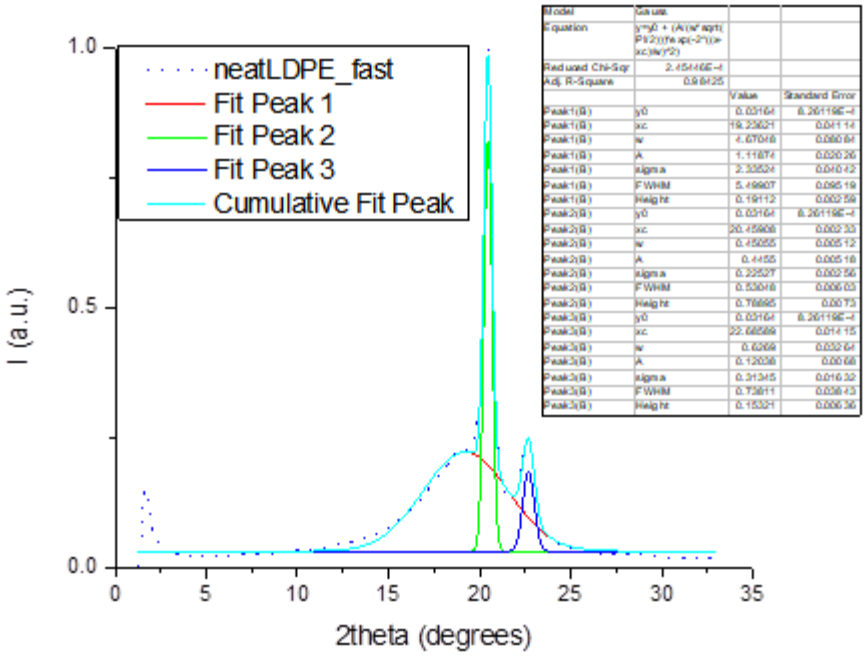

Figure A.12: XRD deconvolution into amorphous (red) and crystalline (green and blue) regions for neatLDPE_fast.

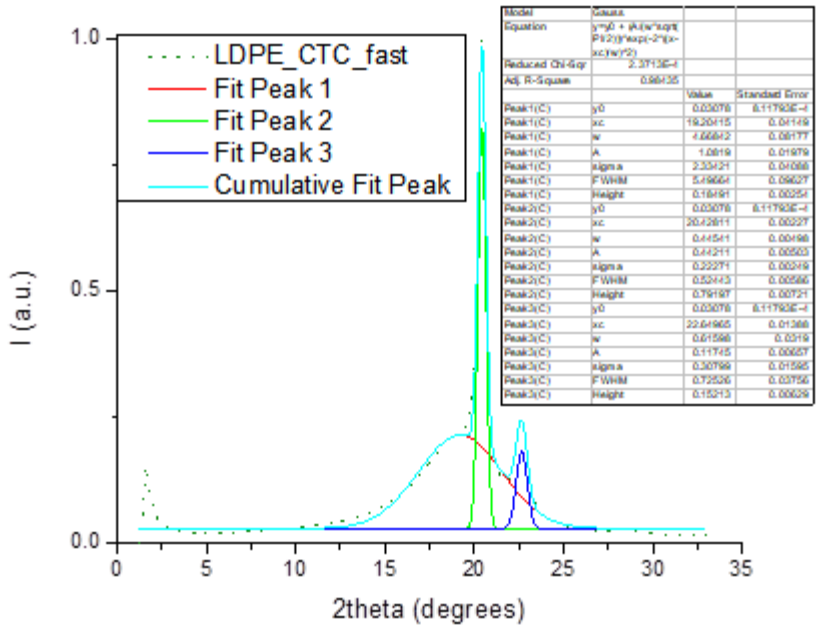

Figure A.13: XRD deconvolution into amorphous (red) and crystalline (green and blue) regions for LDPE_CTC_fast.

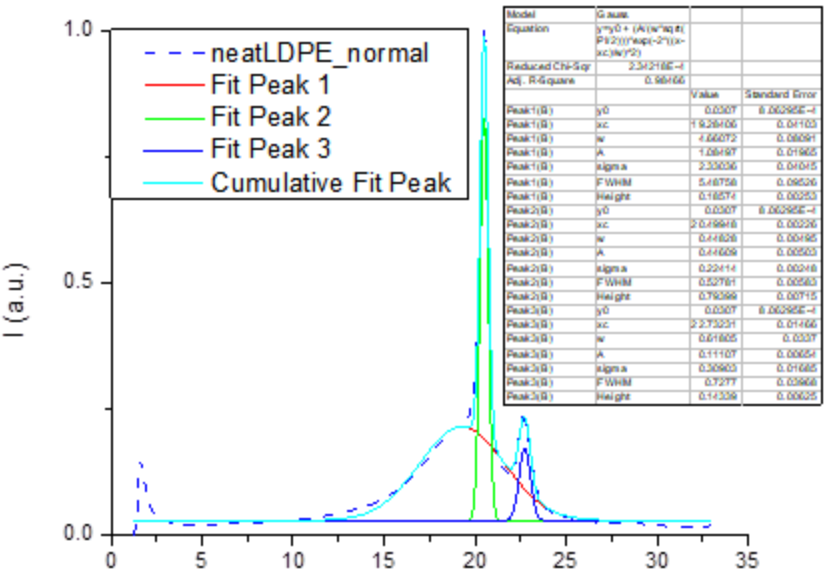

Figure A.14: XRD deconvolution into amorphous (red) and crystalline (green and blue) regions for neatLDPE_normal.

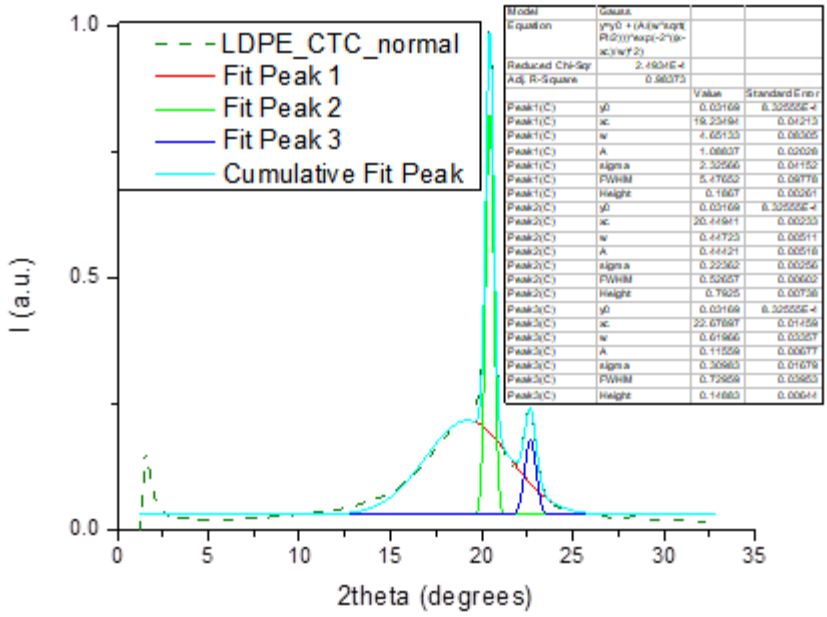

Figure A.15: XRD deconvolution into amorphous (red) and crystalline (green and blue) regions for LDPE_CTC_normal.

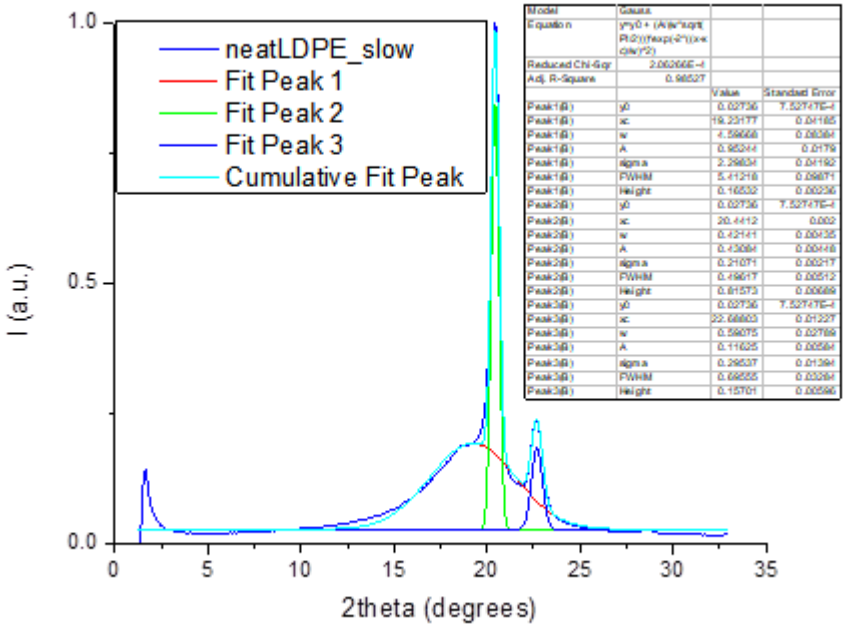

Figure A.16: XRD deconvolution into amorphous (red) and crystalline (green and blue) regions for neatLDPE_slow.

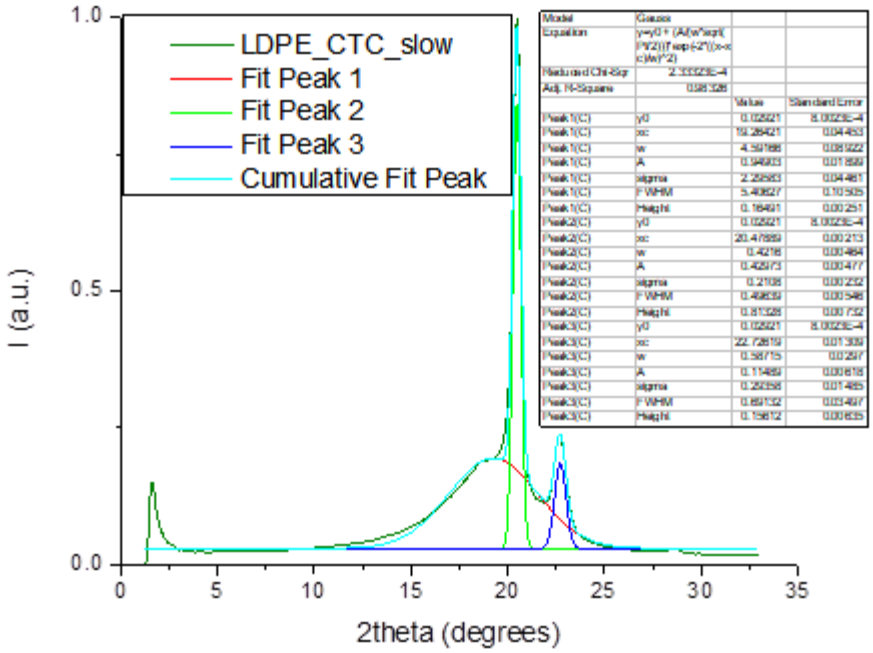

Figure A.17: XRD deconvolution into amorphous (red) and crystalline (green and blue) regions for LDPE_CTC_slow.

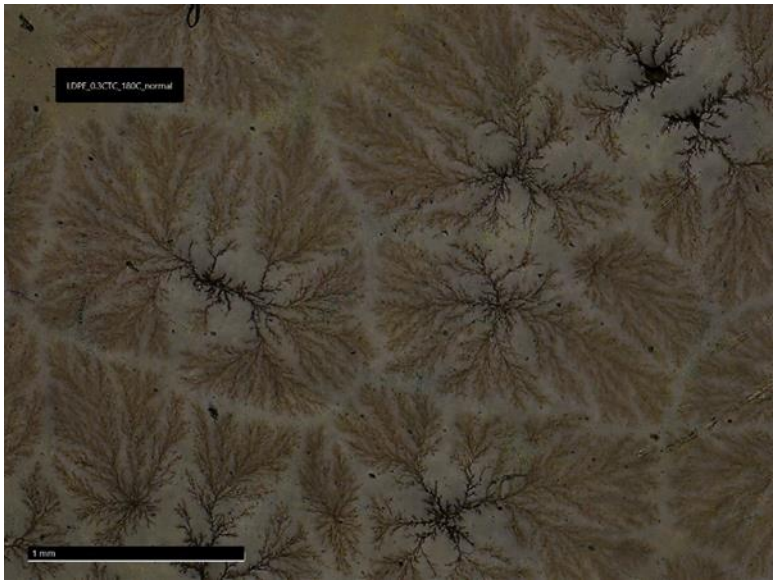

Figure A.18: LDPE_0.3CTC_180C_normal areas with unusually high CTC branch density.

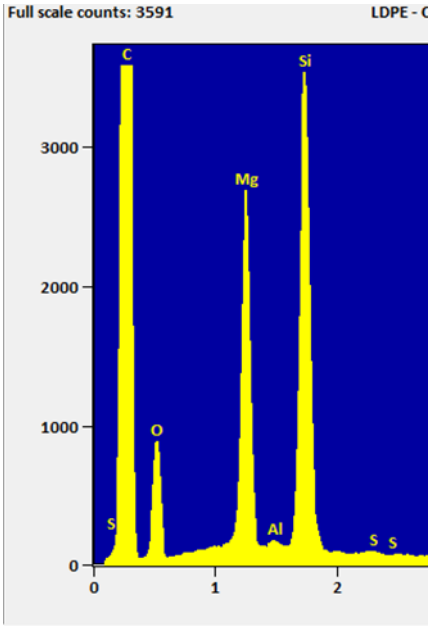

Element Line		Element Wt. %	Wt. % Error +
C	K	74.87	0.36
O	K	12.78	0.27
Mg	K	5.27	0.03
Al	K	0.08	0.02
Si	K	6.95	0.05
S	K	0.05	0.01
Total		100	

Figure A.19: EDX spectrum and results of LDPE_CTC_slow sample.

REFERENCES

(1) Morokuma, K. Why Do Molecules Interact? The Origin of Electron Donor-Acceptor Complexes, Hydrogen Bonding, and Proton Affinity. *Acc. Chem. Res.* **1977**, *10* (8), 294–300. https://doi.org/10.1021/ar50116a004.

(2) Poleschchuk, O. K.; Maksyutin, Y. K. Charge Transfer in Complexes of the Donor-Acceptor Type. *Russ. Chem. Rev.* **1976**, No. 45, 2097–2120.

(3) Benjamin W Gung, D. of C. B. Electronegativity and Electron-donor-acceptor Complexes.

(4) Goetz, K. P.; Vermeulen, D.; Payne, M. E.; Kloc, C.; McNeil, L. E.; Jurchescu, O. D. Charge-Transfer Complexes: New Perspectives on an Old Class of Compounds. *J. Mater. Chem. C* **2014**, *2* (17), 3065–3076. https://doi.org/10.1039/c3tc32062f.

(5) Kryszewski, M.; Jeszka, J. K.; Ulański, J.; Tracz, A. Structure and Electrical Properties of Polymers with Amorphous and Crystalline Dopants. *Pure Appl. Chem.* **1984**, *56* (3), 355–368.

(6) Liu, H.; Li, J.; Lao, C.; Huang, C.; Li, Y.; Wang, Z. L.; Zhu, D. Morphological Tuning and Conductivity of Organic Conductor Nanowires. *Nanotechnology* **2007**, *18* (49), 495704. https://doi.org/10.1088/0957-4484/18/49/495704.

(7) Tracz, A.; Ulański, J.; Kryszewski, M. Conditions for Reticulate Crystalline Doping of Polymer with Charge Transfer Complexes. *Polym. J.* **1983**, *15* (9), 635–639.

(8) Dafne, E.; Rocco, D. *Diffusion Limited Aggregation*; 2009.

(9) Odom, S. A.; Caruso, M. M.; Finke, A. D.; Prokup, A. M.; Ritchey, J. A.; Leonard, J. H.; White, S. R.; Sottos, N. R.; Moore, J. S. Restoration of Conductivity with

TTF-TCNQ Charge-Transfer Salts. *Adv. Funct. Mater.* **2010**, *20* (11), 1721–1727. https://doi.org/10.1002/adfm.201000159.

(10) Marszalek, T.; Nosal, A.; Pfattner, R.; Jung, J.; Kotarba, S.; Mas-Torrent, M.; Krause, B.; Veciana, J.; Gazicki-Lipman, M.; Crickert, C.; et al. Role of Geometry, Substrate and Atmosphere on Performance of OFETs Based on TTF Derivatives. *Org. Electron. physics, Mater. Appl.* **2012**, *13* (1), 121–128. https://doi.org/10.1016/j.orgel.2011.10.001.

(11) Tsutsumi, J.; Matsui, H.; Yamada, T.; Kumai, R.; Hasegawa, T. Generation and Diffusion of Photocarriers in Molecular Donor-Acceptor Systems: Dependence on Charge-Transfer Gap Energy. *J. Phys. Chem. C* **2012**, *116* (45), 23957–23964. https://doi.org/10.1021/jp308720d.

(12) Tsutsumi, J.; Yamada, T.; Matsui, H.; Haas, S.; Hasegawa, T. Competition between Charge-Transfer Exciton Dissociation and Direct Photocarrier Generation in Molecular Donor-Acceptor Compounds. *Phys. Rev. Lett.* **2010**, *105* (22), 1–4. https://doi.org/10.1103/PhysRevLett.105.226601.

(13) Alves, H.; Pinto, R. M.; MaçÔas, E. S. Photoconductive Response in Organic Charge Transfer Interfaces with High Quantum Efficiency. *Nat. Commun.* **2013**, *4* (May). https://doi.org/10.1038/ncomms2890.

(14) Domercq, B.; Grasso, C.; Maldonado, J. L.; Halik, M.; Barlow, S.; Marder, S. R.; Kippelen, B. Electron-Transport Properties and Use in Organic Light-Emitting Diodes of a Bis(Dioxaborine)Fluorene Derivative. *J. Phys. Chem. B* **2004**, *108* (25), 8647–8651. https://doi.org/10.1021/jp036779r.

(15) Murakami, Y.; Horiuchi, S.; Tokura, Y.; Kumai, R.; Kagawa, F.; Kobayashi, K.

Electronic Ferroelectricity in a Molecular Crystal with Large Polarization Directing Antiparallel to Ionic Displacement. *Phys. Rev. Lett.* **2012**, *108* (23), 1–5. https://doi.org/10.1103/physrevlett.108.237601.

(16) Kagawa, F.; Horiuchi, S.; Matsui, H.; Kumai, R.; Onose, Y.; Hasegawa, T.; Tokura, Y. Electric-Field Control of Solitons in a Ferroelectric Organic Charge-Transfer Salt. *Phys. Rev. Lett.* **2010**, *104* (22), 1–4. https://doi.org/10.1103/PhysRevLett.104.227602.

(17) Tokunaga, M.; Kagawa, F.; Fujioka, J.; Tokura, Y.; Horiuchi, S. Ferroelectricity in a One-Dimensional Organic Quantum Magnet. *Nat. Phys.* **2010**, *6* (3), 169–172. https://doi.org/10.1038/nphys1503.

(18) Lee, T.-H.; Huang, W.-S.; Guo, T.-F.; Huang, J. C. A.; Li, J.-H.; Wen, T.-C.; Hu, B. Magnetoconductance Responses in Organic Charge-Transfer-Complex Molecules. *Appl. Phys. Lett.* **2011**, *99* (7), 073307. https://doi.org/10.1063/1.3627170.

(19) Liu, H.; Zhao, Q.; Li, Y.; Liu, Y.; Lu, F.; Zhuang, J.; Wang, S.; Jiang, L.; Zhu, D.; Yu, D.; et al. Field Emission Properties of Large-Area Nanowires of Organic Charge-Transfer Complexes. *J. Am. Chem. Soc.* **2005**, *127* (4), 1120–1121. https://doi.org/10.1021/ja0438359.

(20) Potember, R. S.; Poehler, T. O.; Cowan, D. O. Electrical Switching and Memory Phenomena in Cu-TCNQ Thin Films. *Appl. Phys. Lett.* **1979**, *34* (6), 405–407. https://doi.org/10.1063/1.90814.

(21) Li, L.; Hu, W.; He, M.; Liu, Y.; Meng, Q.; Tang, Z. Device Arrays: Mass-Production of Single-Crystalline Device Arrays of an Organic Charge-Transfer

Complex for Its Memory Nature (Small 4/2012). *Small* **2012**, *8* (4), 478–478. https://doi.org/10.1002/smll.201290026.

(22) Jose, J. P.; Thomas, S.; Joseph, K.; Malhotra, S. K.; Goda, K.; Sreekala, M. S. Part One: Introduction to Polymer Composites. In *Polymer Composites*; 2012; Vol. 1, pp 1–16. https://doi.org/10.1002/9783527645213.

(23) Ahmad, F. N.; Jaafar, M.; Palaniandy, S.; Azizli, K. A. M. Effect of Particle Shape of Silica Mineral on the Properties of Epoxy Composites. *Compos. Sci. Technol.* **2008**, *68* (2), 346–353. https://doi.org/10.1016/j.compscitech.2007.07.015.

(24) Miyasaka, T. Effect of Shape and Photo Size Cure of Silanated Composite Fillers Resins on Mechanical Properties of Experimental Photo Cure Composite Resins. *Dent. Mater. J.* **1996**, *15* (2), 98–110.

(25) Ma, R.; Li, W.; Huang, M.; Feng, M.; Liu, X. The Reinforcing Effects of Dendritic Short Carbon Fibers for Rigid Polyurethane Composites. *Compos. Sci. Technol.* **2019**, *170* (October 2018), 128–134. https://doi.org/10.1016/j.compscitech.2018.11.047.

(26) Pukánszky, B.; Fekete, E. Adhesion and Surface Modification. *Miner. Fill. Thermoplast. I* **2007**, *139*, 109–153. https://doi.org/10.1007/3-540-69220-7_3.

(27) Akovali, G. *The Interfacial Interactions in Polymeric Composites*; Kluwer Academic Publishers, 1992.

(28) DeArmitt, C.; Hancock, M. Chapter 8 - Filled Thermoplastics. In *Particulate-Filled Polymer Composites*; 2003; pp 357–424.

(29) Sharpe, L. H. Some Thoughts about the Mechanical Response of Composites†. *J. Adhes.* **1974**, *6* (1–2), 15–21. https://doi.org/10.1080/00218467408072236.

(30) Sharpe, L. H. Some Fundamental Issues in Adhesion: A Conceptual View. *J. Adhes.* **1998**, *67* (1–4), 277–289. https://doi.org/10.1080/00218469808011112.

(31) Zhang, S.; Wang, H.; Xu, D.; Yang, W.; Tang, P.; Bin, Y. Study of Crystallization Behavior of Neat Poly(Vinylidene Fluoride) and Transcrystallization in Carbon Fiber/Poly(Vinylidene Fluoride) Composite under a Temperature Gradient. *J. Appl. Polym. Sci.* **2016**, *133* (26), 2–13. https://doi.org/10.1002/app.43605.

(32) Kiss, A.; Fekete, E.; Pukánszky, B. Aggregation of CaCO3 Particles in PP Composites: Effect of Surface Coating. *Compos. Sci. Technol.* **2007**, *67* (7–8), 1574–1583. https://doi.org/10.1016/j.compscitech.2006.07.010.

(33) Liu, F.; Wang, R.; Cheng, Y.; Jiang, X.; Zhang, Q.; Zhu, M. Polymer Grafted Hydroxyapatite Whisker as a Filler for Dental Composite Resin with Enhanced Physical and Mechanical Properties. *Mater. Sci. Eng. C* **2013**, *33* (8), 4994–5000. https://doi.org/10.1016/j.msec.2013.08.029.

(34) Sobieraj, M. C.; Rimnac, C. M. *Development and Application of the Notched Tensile Test to UHMWPE*, Third Edit.; Elsevier Inc., 2015. https://doi.org/10.1016/B978-0-323-35401-1.00037-5.

(35) Dorigato, A.; Dzenis, Y.; Pegoretti, A. Filler Aggregation as a Reinforcement Mechanism in Polymer Nanocomposites. *Mech. Mater.* **2013**, *61*, 79–90. https://doi.org/10.1016/j.mechmat.2013.02.004.

(36) Dzenis, Y. Effect of Aggregation of a Dispersed Rigid Filler on the Elastic Characteristics of a Polymer Composite. *Mech. Comp. Mater.* **1986**, *22*, 14–22.

(37) Yang, J.; Han, C. R.; Duan, J. F.; Xu, F.; Sun, R. C. Interaction of Silica Nanoparticle/Polymer Nanocomposite Cluster Network Structure: Revisiting the

Reinforcement Mechanism. *J. Phys. Chem. C* **2013**, *117* (16), 8223–8230. https://doi.org/10.1021/jp400200s.

(38) Zare, Y. Study of Nanoparticles Aggregation/Agglomeration in Polymer Particulate Nanocomposites by Mechanical Properties. *Compos. Part A Appl. Sci. Manuf.* **2016**, *84*, 158–164. https://doi.org/10.1016/j.compositesa.2016.01.020.

(39) Davris, T.; Mermet-Guyennet, M. R. B.; Bonn, D.; Lyulin, A. V. Filler Size Effects on Reinforcement in Elastomer-Based Nanocomposites: Experimental and Simulational Insights into Physical Mechanisms. *Macromolecules* **2016**, *49* (18), 7077–7087. https://doi.org/10.1021/acs.macromol.6b00844.

(40) Tauban, M.; Delannoy, J. Y.; Sotta, P.; Long, D. R. Effect of Filler Morphology and Distribution State on the Linear and Nonlinear Mechanical Behavior of Nanofilled Elastomers. *Macromolecules* **2017**, *50* (17), 6369–6384. https://doi.org/10.1021/acs.macromol.7b00974.

(41) Chaudhary, D. S.; Jollands, M. C.; Cser, F. Crystallinity of Polypropylene-Silica Ash Composites Affected by the Mixing Conditions - DSC Studies. *Polym. Polym. Compos.* **2004**, *12* (5), 383–398.

(42) Huang, X.; Xie, F.; Xiong, X. Surface-Modified Microcrystalline Cellulose for Reinforcement of Chitosan Film. *Carbohydr. Polym.* **2018**, *201* (August), 367–373. https://doi.org/10.1016/j.carbpol.2018.08.085.

(43) Xiao, L.; Mai, Y.; He, F.; Yu, L.; Zhang, L.; Tang, H.; Yang, G. Bio-Based Green Composites with High Performance from Poly(Lactic Acid) and Surface-Modified Microcrystalline Cellulose. *J. Mater. Chem.* **2012**, *22* (31), 15732–15739. https://doi.org/10.1039/c2jm32373g.

(44) Li, B.; Hu, Q.; Wang, M.; Shen, J. Preparation of Chitosan / Hydroxyapatite Nanocomposite with Layered Structure via In-Situ Compositing. *Key Eng. Mater.* **2005**, *289*, 211–214. https://doi.org/10.4028/www.scientific.net/KEM.288-289.211.

(45) Li, K.; Tong, L.; Yang, R.; Wei, R.; Liu, X. In-Situ Preparation and Dielectric Properties of Silver-Polyarylene Ether Nitrile Nanocomposite Films. *J. Mater. Sci. Mater. Electron.* **2016**, *27* (5), 4559–4565. https://doi.org/10.1007/s10854-016-4331-x.

(46) Selim, A.; Valentínyi, N.; Nagy, T.; Toth, A. J. Effect of Silver-Nanoparticles Generated in Poly (Vinyl Alcohol) Membranes on Ethanol Dehydration via Pervaporation. *Chinese J. Chem. Eng.* **2018**, #pagerange#. https://doi.org/10.1016/j.cjche.2018.11.002.

(47) Caro, J.; Fraxedas, J.; Gorostiza, P.; Sanz, F. Nanomechanical Properties of Molecular Organic Thin Films. *J. Vac. Sci. Technol. A Vacuum, Surfaces, Film.* **2002**, *19* (4), 1825–1828. https://doi.org/10.1116/1.1368662.

(48) Pouget, J. P.; Shaprio, S. M.; Shirane, G.; Garito, A. F.; Heeger, A. J. Elastic- and Inelastic-Neutron-Scattering Study of Tetrathiafulvalenium-Tetracyanoquinodimethanide (TTF-TCNQ): New Rsesults. *Phys. Rev. B* **1979**, *91* (4), 1792–1799.

(49) Filhol, A.; Bravic, G.; Gaultier, J.; Chasseau, D.; Vettier, C. Room- and High-Pressure Neutron Structure Determination of Tetrathiafulvalene-7,7,8,8-Tetracyano-p-Quinodimethane (TTF-TCNQ). Thermal Expansion and Isothermal Compressibility. *Acta Crystallogr. Sect. B Struct. Crystallogr. Cryst. Chem.* **1981**,

37, 1225.

(50) Tiedje, T.; Haering, R. R.; Jericho, M. H.; Roger, W. A.; Simpson, A. Temperature Dependence of Sound Velocities in TTF-TCNQ. *Solid State Commun.* **1977**, *23*, 713–718.

(51) Ashby, M. Material and Process Charts. In *The CES EduPack Resource Booklet 2*; 2010; p 5.

(52) Lavrenova, A. Mechanochemistry Based on Supramolecular Interactions, University of Fribourg, 2016.

(53) Van De Wouw, H. L.; Chamorro, J.; Quintero, M.; Klausen, R. S. Opposites Attract: Organic Charge Transfer Salts. *J. Chem. Educ.* **2015**, *92* (12), 2134–2139. https://doi.org/10.1021/acs.jchemed.5b00340.

(54) Mathot, V. B. *Calorimetry and Thermal Analysis of Polymers*; Hanser Publishers, 1994.

(55) Monshi, A.; Foroughi, M. R. Modified Scherrer Equation to Estimate More Accurately Nano-Crystallite Size Using XRD. *World J. Nano Sci. Eng.* **2012**, *2*, 154–160. https://doi.org/10.4236/wjnse.2012.23020.